galaxies

MDPI

Article

Projection-Enhanced Disk Breaks: Evidence from Deep Photometric Decomposition

Sergey S. Savchenko [1,2,*], Ilia V. Chugunov [1,3], Alexander A. Marchuk [1,2], Vladimir P. Reshetnikov [1,2], Matvey D. Kozlov [1,2], Dmitry I. Makarov [1,4], Aleksandra V. Antipova [1,4] and Anastasia M. Sypkova [1,2]

1 Central (Pulkovo) Astronomical Observatory of RAS, Pulkovskoye Chaussee 65/1, 196140 St. Petersburg, Russia
2 Saint Petersburg State University, 7/9 Universitetskaya nab., 199034 St. Petersburg, Russia
3 Sternberg Astronomical Institute, Lomonosov Moscow State University, Universitetsky Pr. 13, 119234 Moscow, Russia
4 Special Astrophysical Observatory, Russian Academy of Sciences, 369167 Nizhnii Arkhyz, Russia
* Correspondence: s.s.savchenko@spbu.ru

Abstract

Radial brightness profiles of disk galaxies often exhibit so-called breaks—locations where their exponential-scale length abruptly changes. Some galaxies have downbending (Type II) breaks, where their brightness decays faster in outer regions, while other have upbending (Type III) breaks, resulting in more extended outer disks or envelopes. Disk radial profiles without any breaks (Type I) appear to constitute a minority. The exact fractions of different break types depend on many galactic parameters—such as Hubble type, stellar mass, spatial environment, and bar presence—and vary significantly across different studies. Another source of discrepancy is the orientation of galaxies: projection effects may play an important role in break detectability. In this work, we utilize DESI Legacy DR10 imaging to perform photometric decomposition of a sample of 375 edge-on galaxies and investigate their radial breaks. We find that the vast majority (≈90%) of disks in our sample have Type II breaks, which is a considerably higher fraction than in many previous works (∼50%). We carefully tested our results to check if observed breaks can be a result of flaring or two-disk composition. We showed that a high fraction of Type II breaks can be attributed to projection effects, which enhance the observed surface brightness of breaks in edge-on galaxies.

Keywords: galaxies: photometry; galaxies: structure

Check for updates

Academic Editor: Lorenzo Iorio

Received: 7 April 2026
Revised: 11 June 2026
Accepted: 30 June 2026
Published: 2 July 2026

Copyright: © 2025 by the authors. Licensee MDPI, Basel, Switzerland. This article is an open access article distributed under the terms and conditions of the Creative Commons Attribution (CC BY) license.

1. Introduction

In the local Universe, about three quarters of bright galaxies have a disk morphology [1,2]. Their general structure can be reasonably well described by two distinct stellar components: a central concentration of stars (bulge) and a rotationally supported flat stellar disk (the latter often hosts other sub-components such as bars and spiral arms). To measure the properties of these components, the method of photometric decomposition is often used (see, for example, [3,4]). The goal of this method is to describe galactic components through analytical functions and to analyze the best-fitting parameters in order to infer the components' properties. To describe the spatial light distribution of a bulge, the usual choice is a single Sérsic function [5]. Disks, on the other hand, often exhibit more complex behavior. In the pioneering works [6,7], the exponential law was shown to be a good approximation to the radial brightness distribution in a disk component. Even though a

simple exponential law is still often used in modern studies on this topic as a default option to describe disks, it was shown in [8–11] and many later works that a considerable fraction of disks cannot be fitted properly with this simple function.

The most common feature in the disk radial brightness distribution is the so-called break: a region where the radial exponential-scale length changes abruptly. If the profile becomes steeper beyond the break radius (i.e., if the exponential-scale length decreases), the galaxy is said to have a Type II profile, also known as a downbending or truncated profile. In the opposite case, the galaxy has a Type III profile (upbending or antitruncated). If no breaks appear, the galaxy has a Type I profile (pure exponential).

Substantial effort has been made to explain the mechanisms of break formation. If a galaxy forms from the collapse of a uniform rotating gas sphere, the resulting disk will have a roughly exponential radial density distribution with a truncation located at about 4.5 exponential scales from its center [12]. Despite its idealized assumptions, the model demonstrates that Type II radial disk breaks can emerge naturally during secular disk evolution. A downside of this model is that the present-day angular momentum distribution in galactic disks may have little in common with that of a protogalactic disk. Non-axisymmetric features such as spiral arms [13,14] and bars [15–17] can effectively redistribute angular momentum in disks, especially at radii close to corotation or Lindblad resonances. This redistribution should smear out various radial features in disks, such as radial gradients of ages or metallicities, including peculiarities of the radial brightness profile. On the other hand, stars near the outer Lindblad resonance (OLR) of a bar effectively exchange angular momentum with it and migrate to larger, nearly round orbits forming rings with radii 2–3 times larger than the bar size [18]. Those rings emerge as a bumpy feature in the azimuthally averaged radial profiles of disks and may appear as a Type II break on a profile (such breaks are dubbed Type II-OLR in [10]).

Another explanation for Type II break formation is that they may be related to an abrupt drop in a star-formation rate beyond the break radius. Such breaks are sometimes called a truncation. Both theoretical [19] and empirical [20] considerations lead to the result that beyond some critical radius, the star-formation rate should decrease rapidly when the gas stability criterion $Q_g(R)$ exceeds unity or the gas surface density $\Sigma_g(R)$ falls below the critical value. This model is supported by both simulations and observations of real galaxies. For example, Ref. [14] carried out a simulation of a star-forming disk evolution. In this simulation, a Type II break appears almost immediately due to a sharp drop in star-formation at the radius, where the gas has not yet cooled enough to effectively form stars. Most of the stars beyond the break were formed in the inner regions and were stirred outward beyond the break by interaction with spiral arms. This process should lead to a U-shaped profile of stellar ages and colors in disks, with a minimum located near the break radius. Indeed, such color profiles are observed in many galaxies [21–23]. It was also noted that the occurrence of Type II breaks is related to the star-formation rate: break frequency increases toward later Hubble types [10,24–28], whereas galaxies with suppressed star-formation (for example, due to the ram pressure stripping or other effects in dense environments) tend to have a reduced fraction of breaks [29–35]. Modern cosmological simulations allow one to track the evolution of radial profiles of stellar and gas surface density along with the star-formation rate on cosmological timescales. In [36] a sample of model galaxies from the Illustris TNG-50 simulation [37] was investigated to determine how Type II breaks form in them. It was shown that the peak of the specific star-formation rate appears near the present-day break radius at $z \approx 0.5$, which leads to an enhanced star assembly compared to both inner and outer regions, effectively producing a break. The same process also reproduces the U-shaped radial curve of stellar ages with the local minimum near the break radius.

There appears to be even less agreement on the explanation of Type III (upbending) breaks. In [24,38] it was noted that Type III breaks can be divided into two subclasses: Type III-s and Type III-d. The distinctive feature of the first subclass is that isophotes become rounder beyond the break radius, which could mean that the excess of light beyond the break is not related to the disk itself, but rather to some spherical component such as a stellar halo [39] or even the extended wings of a bright bulge [40]. In the case of Type III-d, the isophotes beyond the break radius have the same shape, which may indicate that this feature is associated with the disk. The behavior of the outer isophotes, on the other hand, is not an unambiguous classification parameter, since for face-on galaxies the isophotes of both disk and spherical components would have the same shape.

The observed frequency of Type II breaks varies significantly among studies: 12^{+3}_{-2}% [30], 25% [29], 42% [28], 48% [10], 50 ± 4% [25], 66% [24], 82 ± 16% [41]. This discrepancy can be caused by various factors: different photometric depths of used imaging, different photometric bands used, differences in sample distribution by Hubble type, spatial environment, stellar mass, bar presence, etc. Another reason is the orientation of galaxies: some samples mainly consist of galaxies oriented close to a face-on orientation, while others contain only edge-on galaxies. Galaxy orientation may greatly impact the detectability of breaks due to projection effects and different line-of-sight integration paths leading to different surface brightness values around break points.

In this work, we investigate a sample of 375 edge-on galaxies in order to determine the occurrence rate of Type II breaks, and we compare these results with previous measurements made for face-on or mildly inclined galaxies by other authors. This will allow us to make a bridge between two distinct samples of galaxies: face-ons and edge-ons. As a source of images we use the DESI Legacy DR10 survey (g, r, and i bands) [42], which is about 1–2 magnitudes deeper than the SDSS [43] survey often used in previous works on this topic. This article is organized as follows. In Section 2, we discuss the implications of projection effects for the observation of breaks in disks viewed at different angles, including face-on and edge-on orientations. In Section 3, we describe our sample of galaxies. In Section 4, we briefly describe our approach to the decomposition. Our results are presented in Section 5, while our main conclusions are summarized in Section 6.

2. Breaks in Face-On and Edge-On Disks

In this section we consider how breaks appear when projected onto the sky plane when a disk is viewed in different orientations, especially in edge-on and face-on orientations as special cases. A simple transparent Type I disk with an exponential profile in both the radial and vertical directions has the following luminosity density as a function of cylindrical coordinates R (distance to the disk center) and z (height above or below the disk plane):

$$\rho(R,z) = \rho_0 \exp\left(-\frac{R}{h_r}\right) \exp\left(-\frac{|z|}{h_z}\right). \tag{1}$$

When viewed face-on, the line-of-sight integration is along the z-axis and reduces the second exponential, so that the observed surface brightness distribution projected onto the sky plane becomes

$$\Sigma_{\text{face}}(R) = 2h_z\rho_0 \exp\left(-\frac{R}{h_r}\right).$$

In the edge-on orientation, the line-of-sight integration is parallel to the disk plane and leads to an Abel transform of a radial part of the density distribution:

$$\Sigma_{\text{edge}}(R) = 2\int_R^\infty \rho_0 \exp\left(-\frac{x}{h_r}\right) \frac{x}{\sqrt{x^2-R^2}} dx = 2\rho_0 R K_1\left(\frac{R}{h_r}\right),$$

where K_1 is a Bessel function of the second kind [44].

If there is a sharp break in the radial law of the volume brightness density, the equation for $\rho(R,z)$ becomes:

$$\rho(R,z) = \begin{cases} \rho_{0,1} \cdot \exp\left(-\frac{R}{h_1}\right) \exp\left(-\frac{|z|}{h_z}\right), & R < R_b \\ \rho_{0,2} \cdot \exp\left(-\frac{R}{h_2}\right) \exp\left(-\frac{|z|}{h_z}\right), & R > R_b, \end{cases} \tag{2}$$

where $\rho_{0,1}$ is the central volume density of an inner disk, and $\rho_{0,2} = \exp\left(R_b\left(\frac{1}{h_2} - \frac{1}{h_1}\right)\right)$ is a central volume density of an outer disk, computed under the assumption that there is no discontinuity at the break radius. The shape of a broken disk is governed, therefore, by two radial scales, an inner one h_1 and an outer one h_2. The break strength can be expressed either by a linear coefficient between inner and outer radial scales ($h_2 = \alpha h_1$) or on a logarithmic scale by defining strength as

$$s = \log_{10}\left(\frac{h_2}{h_1}\right) \tag{3}$$

(see, e.g., [40,45]). Negative values correspond to Type II breaks and positive values to Type III breaks, and the larger the absolute value, the more pronounced the break is.

Again, when viewed face-on, the line-of-sight integration along the vertical direction of the disk yields a projected surface brightness distribution with an exponential decay in the radial direction and a sharp break:

$$\Sigma_{\text{face}}(R) = \begin{cases} 2h_z\rho_{0,1} \exp\left(-\frac{R}{h_1}\right), & R < R_b \\ 2h_z\rho_{0,2} \exp\left(-\frac{R}{h_2}\right), & R > R_b. \end{cases} \tag{4}$$

The picture becomes more complicated when a disk is viewed edge-on. In this case, the line-of-sight integration along the disk midplane inside the break radius mixes light from the inner and outer disks. Figure 1 schematically illustrates this effect. This figure shows a view of a disk that has a break at the break radius R_b and three lines of sight: the one that lies inside the break radius (LOS_1), the one that passes exactly through the break radius (LOS_2), and the one that lies outside the break radius (LOS_3). Thus, LOS_1 integrates fluxes from both the inner and outer disks, whereas LOS_2 and all outer lines of sight, including LOS_3, integrate only through the outer disk.

Analytically this can be expressed in the following form:

$$\Sigma_{\text{edge}}(R) = \begin{cases} 2\int_R^{R_b} \rho_{0,1} \exp\left(-\frac{x}{h1}\right) \frac{x}{\sqrt{x^2-R^2}}\, dx + 2\int_{R_b}^{\infty} \rho_{0,2} \exp\left(-\frac{x}{h2}\right) \frac{x}{\sqrt{x^2-R^2}}\, dx, & R < R_b \\ 2\int_R^{\infty} \rho_{0,2} \exp\left(-\frac{x}{h2}\right) \frac{x}{\sqrt{x^2-R^2}}\, dx, & R > R_b. \end{cases} \tag{5}$$

Two integrals (for the inner and outer disks) contribute in the region $R < R_b$, while only the outer disk contributes in the region $R > R_b$. Unfortunately, the integrals in (5) cannot be solved analytically and for $R < R_b$ they cannot be reduced to well-documented Bessel functions. Nevertheless, some important conclusions can be drawn regarding the appearance of breaks in face-on vs. edge-on orientations.

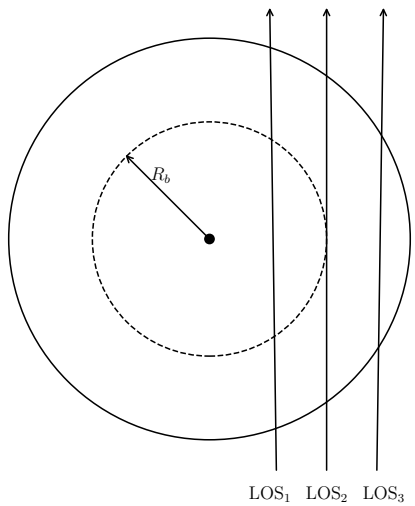

Figure 1. A schematic face-on view of a galaxy, with three parallel lines of sight piercing it at three distinct points: LOS$_1$ lies inside the break radius, LOS$_2$ passes exactly through the break radius, and LOS$_3$ lies outside of the break radius. It is easy to see that the surface brightness at the locations of LOS$_2$ and LOS$_3$ is governed only by the outer disk density distribution.

First, in the edge-on orientation the break appears smoother and its observed location shifts towards the galactic center. This happens because inside the true break radius (LOS$_1$ in Figure 1), a weighted average of the inner and outer disks is observed, so the effective observed exponential scale lies somewhere between the scale lengths of the inner and outer disks. As R increases, the weight of the inner disk decreases, and the outer disk starts to dominate the total observed flux. At $R = R_b$ and farther from the galactic center (LOS$_2$ and LOS$_3$ in Figure 1), only the outer disks contributes to the observed surface brightness. This means that the observed transition from the inner to the outer disk in the radial surface brightness distribution should start before R_b and finish at R_b. To illustrate this effect, the radial surface brightness distributions for the same disk with $h_2 = 0.25h_1$ and $R_b = 4h_1$ are plotted in Figure 2 for the face-on and edge-on orientations. It is seen that the transition between the inner and outer disks in the edge-on orientation appears smoother and occurs somewhat inside the true value of R_b. This implies that simple linear piecewise fits to two disks should lead to underestimation of the R_b value (along with the overestimation of radial-scale lengths, as noted in [46,47]).

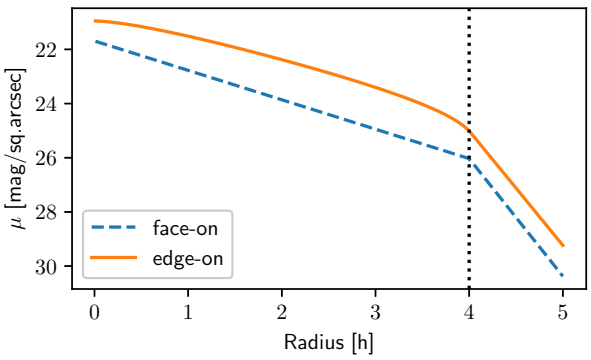

Figure 2. Radial surface brightness for an edge-on and a face-on disk with the same parameters (surface brightness of a model scaled such that for a face-on disk, $\mu(0) = 21.7$ mag/sq.arcsec).

The second point is that, due to projection effects, disks in edge-on orientation should have higher values of surface brightness at the same galactocentric distances than the same disks viewed face-on (at least if one considers the disks to be transparent). The difference is larger for thinner galaxies because for them the face-on line-of-sight integration results in

lower values. By plugging R_b into (4) and (5) and taking the ratio, one can find how much the surface brightness at the break point is higher in the edge-on orientation than when the same disk is viewed face-on:

$$\frac{\Sigma_{\text{edge}}(R_b)}{\Sigma_{\text{face}}(R_b)} = \frac{R_b}{h_z} K_1\left(\frac{R_b}{h_2}\right) \exp\left(\frac{R_b}{h_2}\right). \tag{6}$$

For example, for a disk with parameters $h_2 = 0.25h_1$, $R_b = 4h_1$, and $h_z = 0.2h_1$, which are common for disk galaxies, this equation gives the ratio $\Sigma_{\text{edge}}(R_b)/\Sigma_{\text{face}}(R_b) = 6.4$, which corresponds to a difference of about two magnitudes. This amplification of the surface brightness of the break point in the edge-on orientation relative to the face-on orientation depends on the shape of the outer disk. All else being equal, a more extended outer disk gives higher observed surface brightness at the break point when viewed edge-on (see Appendix B for more details). This should lead to a systematic shift: in edge-on disks, stronger downbending breaks (lower h_2 values) should appear, on average, at lower surface brightnesses, whereas stronger upbending breaks (higher h_2 values) should appear at higher surface brightnesses.

This result cannot be generalized analytically for arbitrary inclinations, but a numerical estimation is possible. Figure 3 shows how the observed surface brightness at the break point depends on inclination for disks with three different ratios of radial to vertical scale (the remaining parameters are the same as in the example above). As expected from Equation (6), thinner disks exhibit a larger ratio of edge-on to face-on surface brightness at the break point (the rightmost points of the curves), and it is clear from the plot that this is true for all inclinations. It is also important to note that the curves are non-linear, and the greatest increase occurs near the high-inclination end.

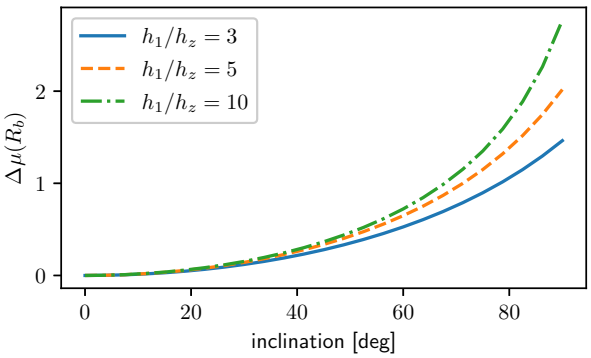

Figure 3. The difference in surface brightness at the break point between an inclined disk and the same disk in the face-on orientation. Different lines correspond disks with different intrinsic thicknesses (see legend).

In the conclusion of this section we would like to note that the approach described above, along with the decomposition method (Section 4), treats a galaxy only within the framework of the observed brightness distribution. But the underlying physical quantity is the volume mass density of stars (or the surface mass density when the galaxy is projected on the sky plane). The direct measurement of the volume mass density from the observed projection of a light distribution is not an easy task for several reasons. First, an inverse Abel transform or other deprojection approach would be necessary to solve this problem [48]. Decomposition using 3D brightness distribution functions as performed in this work can also give information about the intrinsic volume density distribution, but the result becomes model- dependent. In any case, in the second stage, a deprojected 3D brightness distribution should be converted into a mass distribution using a mass-to-light rule (like [49,50]), which becomes an additional source of uncertainty, especially if the conversion is performed using

optical magnitudes. Still, if performed carefully, this would provide interesting insights about disks, since it has already been proven that their brightness and mass distributions do not necessarily coincide [21,28,39]. But this kind of analysis goes beyond the scope of this article.

3. The Sample

The main task of this study—the detection of disk breaks in edge-on galaxies—requires a statistically significant sample of galaxy images. Since breaks are usually observed in the outer regions of disks, where the surface brightness is relatively low (and beyond the Type II break a disk fades out even faster), we decided to use the DESI Legacy Survey (https://www.legacysurvey.org/ (accessed on 29 June 2026)) [42] as our source of images. By computing statistics in randomly selected 10×10 arc-second boxes in the object-free areas of random fields, we estimate the 3σ limiting depth in the g-band to be 28.98 ± 0.41 mag per sq. arcsec (specified uncertainty is a three-sigma standard deviation of the limiting depth computed over a sample of random fields).

We build our sample using a combination of the EGIPS [51] and RFGC [52] catalogs of galaxies viewed close to edge-on. The EGIPS catalog was created using an artificial neural network classifier applied to the Pan-STARRS1 survey [53]. We extended this catalog with the RFGC galaxies to cover the southern part of the sky, since the Pan-STARRS1 survey only contains regions of the sky north of $\delta = -30^\circ$. To refine this combined catalog and obtain a smaller sample of galaxies viewed very close to edge-on orientation, we performed a visual examination of the images (The EGIPS database contains information about neural network scores that could in principle be used as a starting point to exclude galaxies that deviate from edge-on orientation, but the RFGC catalog does not have such a parameter, so for consistency we decided to opt for visual inspection of both parent samples). We downloaded RGB images of all EGIPS galaxies from the DESI Legacy footprint, and each galaxy was inspected by five randomly selected participants from the author list. The decision was made based on the symmetry of the bulge appearance (in an edge-on flat galaxy the bulge should be divided into two equal parts by the disk plane), the dust lane shape (should appear as a straight line and divide the stellar disk into equal parts), and the overall appearance of outer isophotes (slightly inclined galaxies demonstrate rounder isophotes in their outer regions). If a galaxy received at least four positive votes out of five, we considered it a genuine edge-on galaxy and included it in our sample. This selection left us with 375 galaxies (301 from EGIPS and 74 from RFGC). According to the EGIPS database, the median r-band axis ratio of our sample galaxies that are included in EGIPS is 0.168, which is somewhat lower than the median axis ratio of the full EGIPS sample, which is 0.210. The lower value of the axis ratio is a result of stricter selection of galaxies regarding their proximity to edge-on orientation. We have not performed any inclination measurements of our galaxies since it is not an easy task for galaxies that are almost edge-on: a usual approach that relies on comparing some average intrinsic axis ratio to an observed one fails when the inclination is close to 90 degrees. We compared the apparent shifts in dust lanes of our galaxies to those of edge-on galaxies that have inclination estimates from radiative transfer decomposition (for example, [54,55]) and concluded that for most of our galaxies the deviation from true edge-on orientation is within $\approx$1 degree.

We downloaded FITS images of all sample galaxies in the g-, r-, and i-bands along with corresponding inverse variance maps via the DESI Legacy cutout service (https://www.legacysurvey.org/viewer/cutout.fits (accessed on 29 June 2026)). We also downloaded the appropriate PSF kernels from the survey web server to build PSF images following the survey guidelines (https://www.legacysurvey.org/dr10/psf/ (accessed on 29 June 2026)). To exclude background and foreground objects and image artifacts from further analysis,

we created mask images using object catalogs generated by the SEXTRACTOR package (2.28.2) [56]. For every passband we ran SEXTRACTOR, loaded its output object catalog as a set of ellipses, excluded the central object (the target galaxy) and multiplied the sizes of all ellipses by 1.5 to properly cover even the outer low-surface-brightness extended wings of bright objects that can be missed by SEXTRACTOR. We displayed the ellipses overlaid on the galaxy image for a visual inspection and possible modifications using the SAOImage DS9 package (8.0.1) [57]. After that we made a binary mask that excludes all pixels inside the ellipses. As the final mask we used the union of all masks created for all photometric bands.

As the final step of the data preparation, we created dust masks to exclude regions of disks heavily contaminated by the dust lane. Dust can greatly affect the observed parameters of galaxies [58–60], especially for edge-on galaxies [61]. Excluding dust-attenuated regions from the analysis is a possible way to reduce the influence of dust (see, for example, [61,62]). In this work, we decided to manually make masks using the SAOImage DS9 package to exclude dust-contaminated regions in the images.

4. The Decomposition

To obtain information about disk breaks in our sample galaxies, we used the algorithm of photometric decomposition. The goal of this approach is to construct a model of a galaxy image using a set of analytical functions, such that each function corresponds to a galactic component. The values of the galactic parameters are inferred from the best-fitting parameters of the model. To do this, we used the IMFIT package (1.9) [4]. This package takes as inputs a galaxy image, a weight map, a masked pixel map, a PSF image, and a configuration file describing a model and the initial parameters, and performs a search for best-fitting values to these parameters.

For our models we adopted the following functions. To describe a central light concentration, we used a Sérsic function [5]. The nature of this central light concentration is somewhat uncertain since it may include multiple different components such as classical bulge, pseudo-bulge, bar, nuclear disk, X-structure, etc., and it is often difficult to separate them based solely on photometry. Instead, they are often fitted as a single combined component, sometimes called a 'photometric bulge' [63]. Probably the most prominent additional component (besides the bulge/pseudo-bulge itself) is an X-structure. Even though it is possible to include it as a separate component [64,65], this would add a considerable number of additional free parameters to the model. In this work we concentrate on the disk shape, and hence, we fit the central concentration only to reduce its impact on the disk component. In the Results section we will mark galaxies where we detect the presence of an X-structure, and where the obtained bulge parameters suffer from this.

For a disk itself, we used two different functions. The first is the function that is described by the Equation (1), used to model disks without noticeable breaks. The second is a function (2) used to model broken disks. Both three-dimensional disk functions are included in the list of standard functions of the IMFIT package, and during the decomposition process they are projected on a picture plane via numerical line-of-sight integration. To decide which of the two disk models to apply to a particular galaxy image, we used the following approach: We started with decomposition using a simple unbroken disk and then inspected visually two-dimensional residual maps (data minus model) and photometric cuts of the data and model made along the galaxy's major axis. If a disk contains a break, its presence is clearly visible during these inspections, and approximate break parameters (break radius and break type) can also be estimated alongside it. We then replaced the simple disk function with a broken disk in the configuration file, taking its radial and vertical scales as initial conditions for a new model. This approach not only allows us to robustly detect disk breaks, but also to build a complex model with a broken disk using a

simpler one as an intermediate step. The procedure described above was applied to the *r*-band first, and then these results were used as initial conditions for the other bands.

Figure 4 demonstrates the results of the decomposition for three galaxies: PGC 90713, PGC 16144, and PGC 49296. The figure shows horizontal slices taken along major axes: blue—the observed brightness distribution, green—the Sérsic function (bulge), red—the BrokenExponentialDisk3D function (disk), and orange—the total model. To exclude dust-contaminated regions (which were masked out), the figure shows the average of two slices taken above and below the dust lane. Figure 5 shows the decomposition results for the same three galaxies in the form of 2D image maps. The left panels for each galaxy show the original images in the *r*-band, with yellow regions indicating parts of the background that the objects mask, red regions representing the manual dust mask, and the white line indicating a scale of 30 arc seconds. The middle panels show the model images, while the right panels show residual "image−model" maps with the dust mask overlaid.

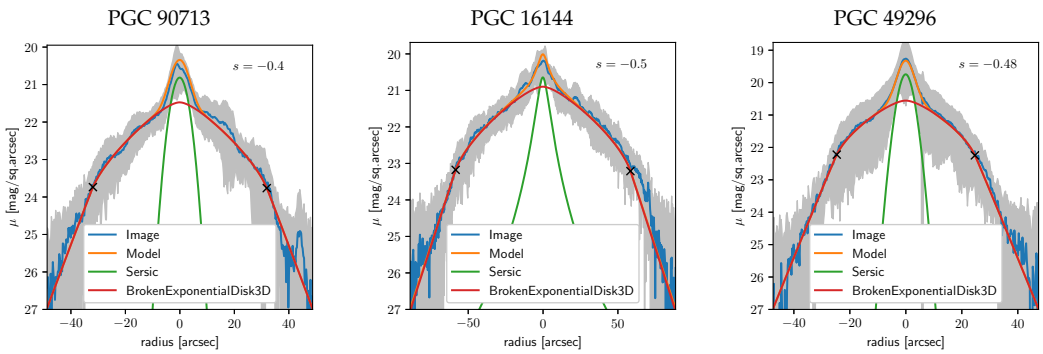

Figure 4. Decomposition results for three galaxies: PGC 90713, PGC 16144, and PGC 49296. Each panel shows photometric slices taken along the galaxy's major axis. Break locations are shown by x-marks. Numbers in top right indicate the break strength (see Equation (3)). To reduce the noise, for each slice we compute the arithmetic mean of surface brightness inside a strip with a width of 1.6 arc seconds (roughly the PSF size). To exclude the dust-attenuated regions, we take two parallel slices above and below the dust lane and compute their average. The blue line shows the observed brightness distribution, orange represents a full model, while green and red show bulge and disk models respectively. The shaded region shows the standard deviation of the observed surface brightness inside a 1.6 arc-second strip.

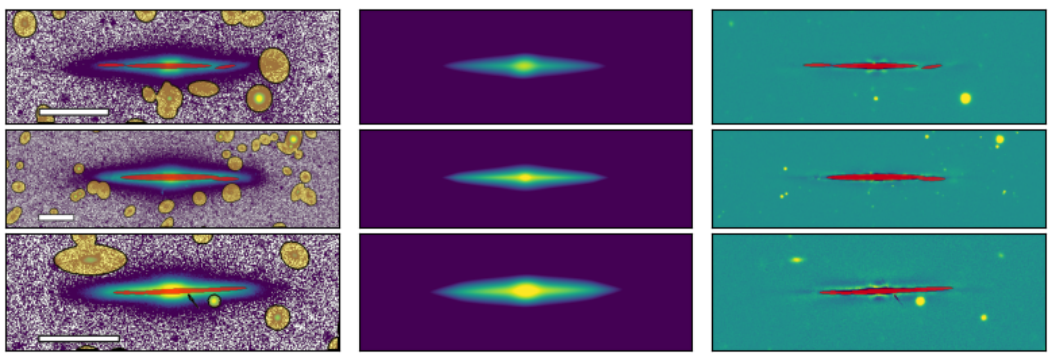

Figure 5. Decomposition results for the same three galaxies as in Figure 4, but shown as 2D image maps. (**Left column**): original images in the *r*-band, with yellow regions indicating the background objects mask; red regions—the manual dust mask. The white line in the bottom left marks a scale of 30″. (**Middle panels**): model image. (**Right panels**): "image−model", with the dust mask overlaid.

5. Results

Figure 6 shows the distributions of the galaxies in our sample according to several parameters inferred from the decomposition. The left panel shows the distribution of

absolute magnitudes in the r-band, which were computed from the integrated magnitudes of bulge and disk models, and luminosity distances to galaxies according to the NED (https://ned.ipac.caltech.edu/ (accessed on 29 June 2026)) (Galactic extinction was corrected following [66]). Since only 310 galaxies in our sample have distance measurements in the NED, absolute magnitudes and stellar masses are computed only for this subsample, and the provided distributions may not reflect the true distribution of a whole sample. The middle panel shows the distribution of our sample galaxies according to the radius of the 27th-magnitude isophote in the r-band. This parameter was computed from the disk models obtained during the decomposition (we neglected the bulges, since surface brightness in the outer regions is dominated by the disks). The right panel shows the distribution of galaxies by stellar mass computed from absolute magnitudes in the g- and r-bands using the calibration from [50]. It can be seen from this panel that the galaxies in our sample have stellar masses from $\sim 10^{9.5}$ to $\sim 10^{11.5}$ $M_\odot$, with a peak at $10^{10.5} M_\odot$; thus they cover a entire mass range characteristic of disk galaxies, and other works on disk breaks often cover a similar mass rage: 10^9–10^{11} $M_\odot$ in [28], 10^9–$10^{11.5}$ $M_\odot$ in [27], $M_* > 10^{9.5}$ in [29]. We note that our mass estimates were obtained using magnitudes from the decomposition, in which we at least partially reduced the impact of dust attenuation by applying dust masks. Dust attenuation is most significant for edge-on galaxies, so our optical fluxes (and hence, the derived stellar masses) should be higher than those obtained from simple aperture photometry. Nevertheless, a small number of the most massive galaxies in our sample (with stellar masses close to $10^{12} M_\odot$) could be outliers due to natural scatter in the measurements and possible systematics in the flux-to-mass calibration.

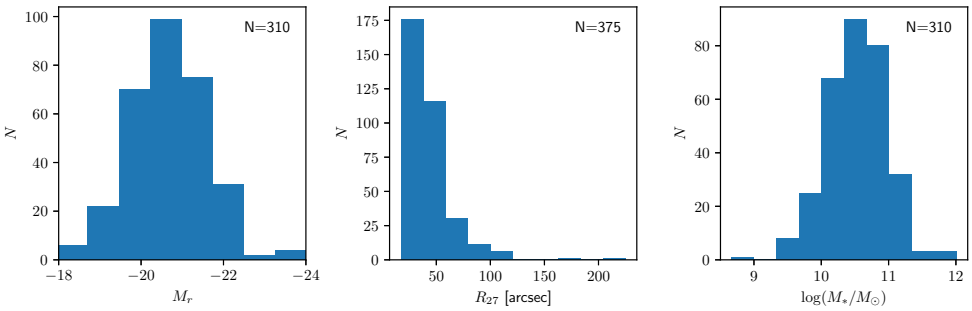

Figure 6. Distribution of sample galaxies by absolute magnitude in the r-band (**left**), radius of 27th-magnitude isophote in the r-band (**middle**), and stellar mass (**right**). Numbers of galaxies for which the corresponding parameter was obtained are shown in the top right corners.

5.1. Fraction of Breaks and Comparison to Previous Works

Out of the total of 375 galaxies in our sample, 33 galaxies ($8.8^{+1.6}_{-1.4}$%) show no radial breaks (Type I), 341 galaxies ($90.9^{+1.4}_{-1.6}$%) exhibit downbending (Type II breaks), and only one galaxy ($0.3^{+0.4}_{-0.2}$%) has an upbending (Type III) break (the uncertainties are 1σ Wilson intervals that were computed using PROPORTION_CONFINT function of STATSMODELS.STATS.PROPORTION Python 3.13.14 package). Figure 7 shows the distributions of the breaks detected in our sample: left panel—break radii normalized by the disk's 27th magnitude isophote, and right panel—surface brightness at the break point (both in the r-band).

The fraction of galaxies with breaks in our sample is considerably higher than in many previous studies, where most estimates find that roughly half of the galaxies host Type II breaks [10,25,28], with some reporting up to 82% [41]. In the following subsections we discuss possible reasons for this discrepancy: impact of the photometric depth, possible disk flaring and an interplay between two disks (thin and thick) with different radial scales.

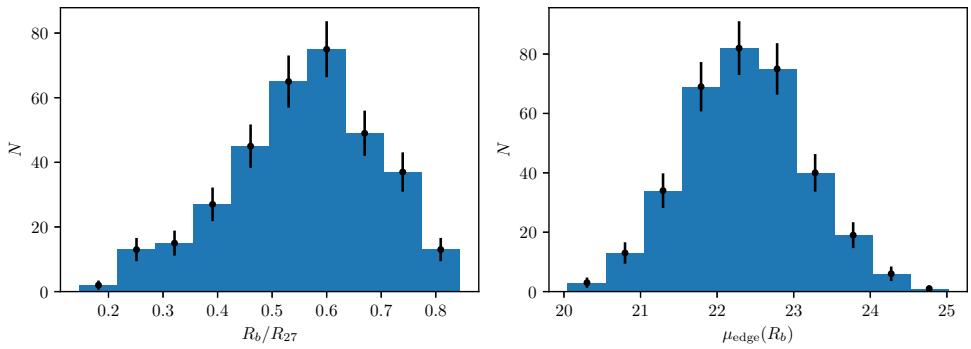

Figure 7. (**Left**): Distribution of the sample break radii normalized by the disk's 27-th magnitude isophote in the *r*-band. (**Right**): Distribution of breaks by the surface brightnesses at the break point in the *r*-band. Error bars show Poisson $\sqrt{N}$ uncertainty.

5.1.1. Impact of Photometric Depth and Disk Orientation

The DESI Legacy DR10 survey used in this work provides considerably deeper imaging compared to many older wide-field surveys. For example, the Sloan Digital Sky Survey, which is often used to investigate breaks in disk galaxies, is almost two magnitudes shallower in the *g*-band: our estimate of its 3σ depth made in 10×10 arc-second squares is 27.17 ± 0.13 magnitudes per square arc second compared to 28.98 ± 0.41 for the DESI Legacy DR10.

A second reason for the higher fraction of breaks detected in this work is that we investigate a sample of edge-on galaxies. As discussed in Section 2, projection effects lead to higher observed surface brightness in edge-on galaxies compared to face-on or mildly inclined ones, and the discrepancy can amount to several magnitudes. This means that more distant regions of galaxies can be probed, where outer breaks may exist. To check this possibility, we recalculate the observed surface brightness at the break point that we obtained (shown on the right panel of Figure 7) into a face-on orientation using Equation (6). This equation can be applied to our galaxies since we also obtained vertical scales of their disks during the decomposition, a quantity necessary for such a computation, which can be obtained robustly only for edge-on galaxies. The resulting distribution is shown in Figure 8 (blue-filled histogram). One can see that the entire distribution has shifted considerably toward lower surface brightness levels, so if the same galaxies were observed face-on, some breaks would be located in faint outer regions, and would hence be difficult to detect. For comparison, we also plot on the same figure the combined results from [10,24]. In these works face-on and mildly inclined galaxies were investigated—i.e., those for which projection effects do not provide favorable conditions for detecting breaks in faint outer regions. We note, however, that this comparison should be treated as only qualitative, since the galaxies in the samples of [10,24] are not strictly face-on oriented, and recalculation of their surface brightness would also be needed, but without the information on their vertical-scale lengths, such correction cannot be performed. On the other hand, from Figure 3 it is clear that this correction is relatively small for disk inclinations below 60 degrees, which were analyzed in these works. Another point is that the samples considered in this work and in [10,24] may differ in distribution based on the environment, Hubble type, stellar mass, and other parameters, which are known to correlate with the fraction of disk breaks. For example, galaxies with lower surface brightness are more likely to be detected if observed edge-on. In any case, from this figure it can be seen that the number of breaks detected in [10,24] drops rapidly for surface brightness levels below ∼25 magnitudes per square arc second, whereas we detect a considerable number of breaks in these faint regions.

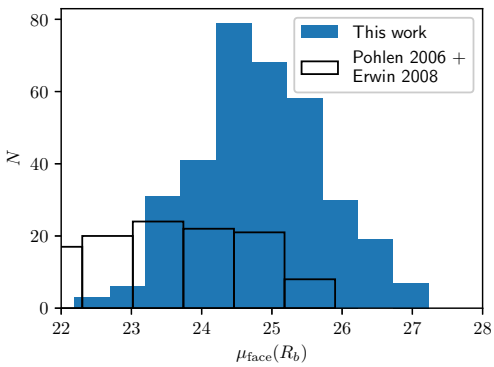

Figure 8. Distribution of surface brightness at the break point obtained in this work and recomputed to a face-on orientation (filled blue), compared with measurements from [10,24] (unfilled black).

Another interesting result from Figure 8 is that on the faint side of the plot the number of breaks detected in [10,24] is, on the contrary, much higher than we detect. This can also be explained as an outcome of projection effects. Breaks in regions of high surface brightness are often related to the outer Lindblad resonances of bars (such breaks are dubbed II.o-OLR in [10]), and the edge-on orientation disfavors their detections because they are smeared out by the projection of the outer disk (see Figure 2) and are also likely to be greatly affected by the dust.

5.1.2. Impact of Flaring

As mentioned in [45], disk flaring may lead to an apparent Type II break in an edge-on galaxy even if the same disk would appear to be Type I when viewed face-on. This happens because the flaring reduces the flux in the disk plane by scattering some fraction of stars to larger heights. In this section, we check if such an effect may affect our results. We start with the equation of a flared (but not broken) disk:

$$\rho(R,z) = \rho_0 \exp\left(-\frac{R}{h_r}\right) \exp\left(-\frac{|z|}{h_z(R)}\right) \frac{h_{z,0}}{h_z(R)}. \tag{7}$$

Here, $h_z(R)$ is a function that describes how the vertical scale depends on radius, and $h_{z,0}$ is a vertical scale of the disk inside the flare onset radius. The last term is needed to keep the total number of stars at a given radius: flaring makes the disk thicker, not more massive (see corresponding equations in [45,67]). By combining this equation with the outer part of a broken disk from Equation (2), we can find the analytical form of $h_z(R)$, i.e., we can find how strong a flare should be to produce the observed strength of a downbending break. If we define break strength such that $h_2 = \alpha h_1$ (with $0 < \alpha < 1$ for a Type II break) and $x = R - R_b$ is the distance from the break position outwards, the solution for $h_z(R)$ would be

$$h_z(x) = \exp\left(\frac{1-\alpha}{\alpha}\frac{x}{h_1}\right) h_{z,0} \tag{8}$$

(see the full derivation of this equation in the Appendix A). And vice versa, if we have flaring in the form of

$$h_z(x) = \exp\left(f\frac{x}{h_1}\right) h_{z,0},$$

with f describing the flaring strength, then the observed break strength would be

$$\alpha = \frac{1}{1+f}. \tag{9}$$

There are several immediate consequences immediately of Equation (8). First of all, to produce an exponential break in radial surface brightness as defined in Equation (2), an *exponential* flaring is needed. *Linear* flaring, which is often reported in the literature (e.g., [68–71]), cannot produce an *exponential* radial break. The second point is that the required flaring strength strongly depends on the break strength. The observations of exponential flare strength for the galaxy, where such measurements are most extensive, do not show values larger than $f = 0.5 \ldots 0.6$ [72–75], so if we take a flare strength of $f = 0.6$ as the most extreme case, we can use Equation (9) to find that the most extreme break would be $h_2 = 0.625 h_1$, or, in terms of logarithmic break strength (see Equation (3)), $s = \log(0.625) = -0.2$. This value is very close to the one obtained in a numerical experiment by [45].

The final note we would like to discuss here is that the relation between the flare strength and the apparent break strength is found for the worst-case scenario: one-dimensional decomposition of a photometric slice taken along the galactic plane (as was studied in [45]). In such a case, the light that left the disk plane due to flaring is completely missed during decomposition. But it is not the case for the two-dimensional decomposition performed in this work. When we perform two-dimensional decomposition, the IMFIT package that takes the whole image as input still captures some fraction of the flared light above and below the disk plane. In other words, the flared light is not missing completely in the case of two-dimensional decomposition. This effect should lead to a lower measured break strength than the one predicted by Equations (8) and (9). To check for this possibility, we performed the following numerical experiment.

We added a function of a flared disk according to Equation (7) to the IMFIT package following the package user guide. Then we created a set of model images of flaring disks with flaring strength f in the range 0 to 0.6. After that we performed two types of decomposition by a single broken disk: one-dimensional decomposition of a photometric slice taken along the disk plane (as in [45]) and two-dimensional decomposition using IMFIT. Then we checked how the measured break strength depends on the input flare strength. The results of this experiment are shown in Figure 9, where the measured break strength is plotted against the input flare strength. Here a solid line shows the analytical prediction of Equation (9), asterisks show results of one-dimensional decomposition, and dots show results of two-dimensional decomposition. As expected, the measured break strength increases with the flaring strength. It is evident that numerical results of one-dimensional decomposition align perfectly along the analytical prediction, which validates our findings. We also note that in two-dimensional decomposition the measured break strength is *lower* than in the one-dimensional case, as we expect, due to partial capturing of flared light by a two-dimensional function.

The main result of this section is that even though stellar disk flaring can indeed produce a Type II break appearance in an edge-on disk, the strength of this effect is not high enough to explain the observed distribution of Type II breaks. Any reasonable flaring strength cannot produce a downbending break stronger than $s \approx -0.2$ during one-dimensional decomposition, and results in even weaker breaks ($s \lessapprox -0.15$) for two-dimensional decomposition. In fact, almost all breaks in galaxies of our sample are stronger than this limit (see Section 5.3). Therefore we do not expect our galaxies to change their break type due to flaring, and rule out flaring as a possible source of the high fraction of Type II disk breaks in our sample.

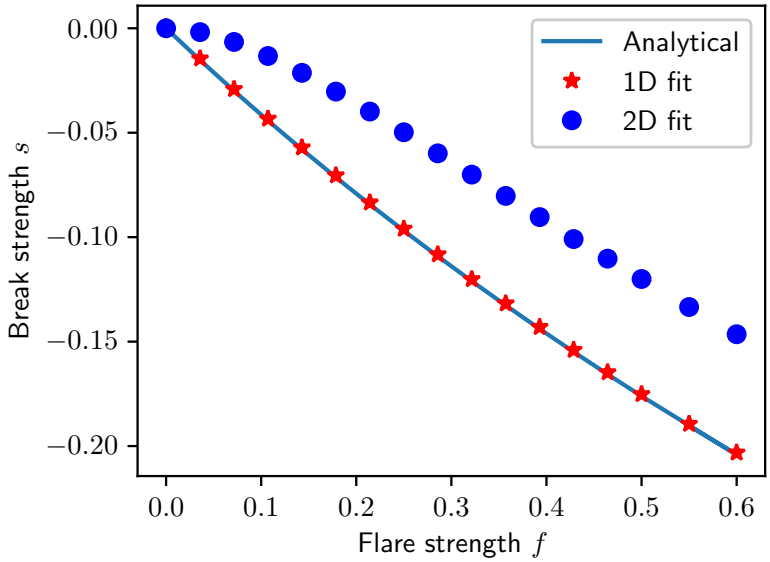

Figure 9. Results of the numerical experiment on the decomposition of a flaring disk by a broken disk model, highlighting how the measured break strength depends on the true value of the flare strength. Solid line: analytical prediction from Equation (9); asterisks: result of one-dimensional decomposition; dots: results of two-dimensional decomposition.

5.1.3. Thin and Thick Disks

So far, we have carried out our analysis considering only a single disk. However, a disk often consist of two components, thin and thick, with different scale heights [76]. If their radial brightness distributions are similar, then a single disk model with free-fitted n may still describe the combination of both of them reasonably well. More importantly for our study, in this case we would correctly obtain the properties of disk break.

However, the thick and thin disks may have different radial scales. For example, if the thick disk (whose central brightness is fainter) has a larger radial scale than the thin component, at the periphery it may overtake the thin disk in brightness, creating the appearance of a Type III radial break [76]. Similarly, the vertical disk profile at larger radii becomes thick-disk-dominated, yielding a higher vertical height and causing apparent flaring. Thus, fitting these two disks with a one-disk model may potentially bias the results regarding break detection.

To examine cases like the one described above, we fit two disks—a thin and a thick one—to the image. Examining images, models, and 2D residual maps, we select nine galaxies that likely have the most prominent thick disks and 10 other random galaxies, and fit them with a model containing a bulge and two disks without breaks. Note that our aim is not to obtain a perfect two-disk model (hence, we do not add breaks) but rather to ensure that our conclusion regarding break statistics is correct.

We compare this two-disk model with the original model, with an example shown in Figure 10. It turns out that, both for the subsample of galaxies with an apparently prominent thick disk and for those without it, the two-disk model almost always has worse fit quality: the two-disk model usually fails to reproduce the appearance of Type II profiles (which are observed in 16 out of 19 galaxies across the two subsamples). In these 16 galaxies, only one has its fit quality improved when two disks are used (and it is a galaxy with a prominent thick disk). The median χ^2 for the 9 galaxies with an apparent thick disk is 1.88 for the original models and 2.31 for the two-disk models, and for the control sample of 10 galaxies these values are 0.97 and 1.16, respectively.

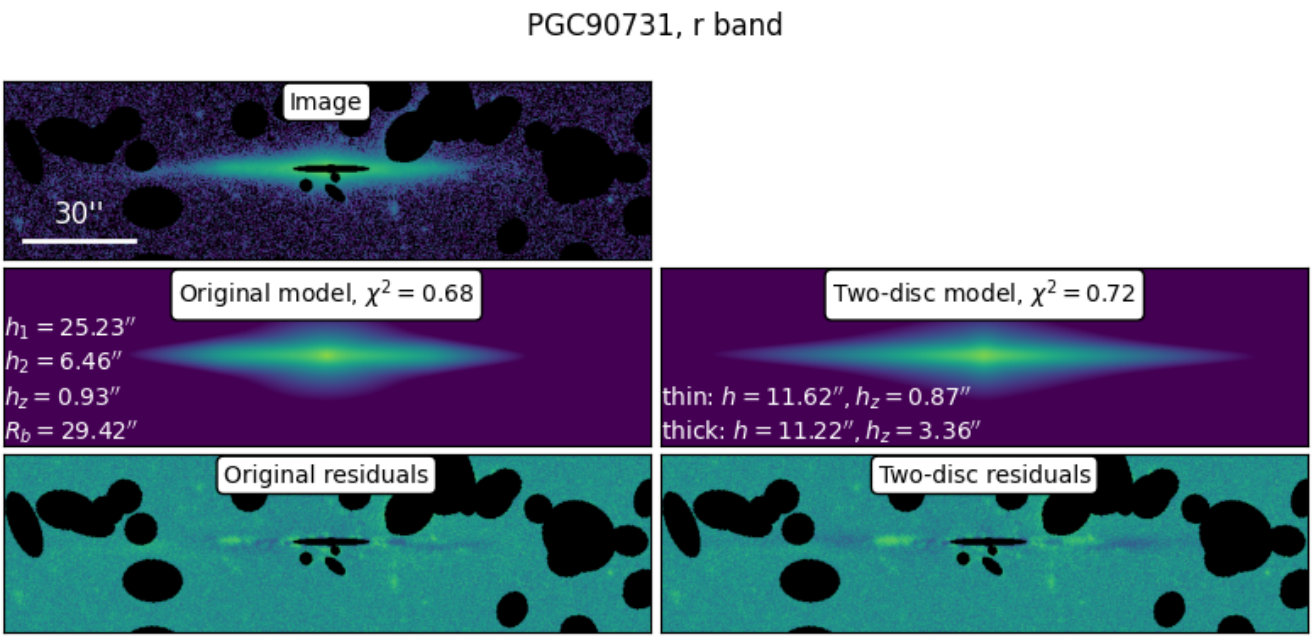

Figure 10. A comparison between our original model containing a single disk with a break (**left column**) and a model with two disks, one thick and one thin (**right column**). From top to bottom: image, model, and residual image. Disk parameters are listed at the corresponding model images.

Again, this analysis does not imply that galaxies in our sample lack thick disk components, but rather it shows that Type II profile appearance cannot be explained by the combination of two disks without breaks. Indeed, if the thick disk has the same or a smaller radial scale than the thin one and both have no breaks, the radial profile would be Type I, defined only by the thin component. Otherwise, the Type III profile could appear as described above. However, for a Type II profile to appear, the more prominent component of the disk has to demonstrate a genuine downbending break. In other words, the observed fraction of Type II profiles is not exaggerated due to the single-disk approach, nor do we miss Type III profiles with a given precision.

5.1.4. More Complex Disk Structures?

Above we investigated two possibilities that could lead to the erroneous attribution of an edge-on galaxy to a broken type: flaring and two-disk composition. In this section we describe another test to check if some complicated dependence of vertical brightness distribution on radius could lead to the false appearance of a broken disk. The idea is to project the vertical light distribution onto a disk plane and check if this projected light distribution still gives the broken radial profile. To do so, we adopt the following approach: First, we rotate an image of a galaxy such that it appears horizontal. Then, for each point in the galaxy plane, we compute the total flux from all pixels above and below this point (taking a stellar mask into account). As a result, we obtain a projection of a galaxy onto an infinitely thin disk. In this projection, we compensate for all irregularities of the vertical brightness distribution such as flaring, because we combine the total light from all heights at any given radius regardless of the underlying vertical brightness distribution. If we observe a radial break in this projected brightness distribution, then it is not an artifact of flaring, a thin–thick disk dichotomy, or any combination of such effects.

The results of this experiment are presented in Figure 11 for four galaxies of our sample that present Type II breaks. For each galaxy, the blue line shows a regular photometric cut taken along the disk plane, and the red line shows the brightness distribution projected onto the disk plane. Both curves are shifted vertically such that the central brightness of one matches that of the other. It is clear from this figure that for all four galaxies the difference between two brightness distributions increases at larger radii, which may indicate radial variations of $h_z(R)$ due to flaring/a thick disk: there is more light at higher altitudes in outer regions of galaxies. This is especially prominent for PGC 763563. But for all galaxies the break persists even in the projected brightness distribution, so we can conclude that these galaxies indeed have downbending breaks. This is also true for all the other galaxies of our sample; we have not found any galaxies where the break disappears on the projected brightness distribution. Finally, we note that in the projected brightness distribution the break strength may be lower because the disk's inner and outer radial scales and break radii depend on height [48], which leads to smearing of the projected profile.

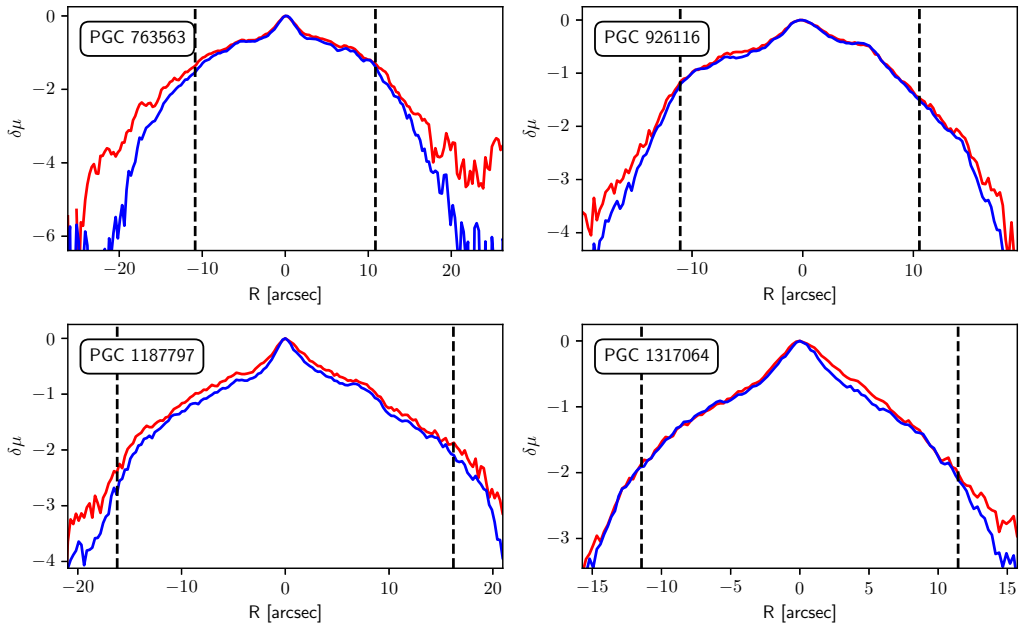

Figure 11. Results of the experiment on brightness projection onto a disk plane are shown for four galaxies with Type II breaks. In each panel, the blue line shows a photometric cut along the disk plane, and the red line shows radial brightness distribution of the projection. Both brightness distributions are shifted vertically such that their peaks match. Vertical axes show brightness fading in stellar magnitudes relative to the peak. Vertical dashed lines show break positions computed from 2D decomposition.

5.2. Outer Disk Scale vs. Surface Brightness at Break Point

As noted in the discussion of Equation (6), when a galaxy is observed edge-on, there should be an artificial projection-induced correlation between the radial-scale length of the outer disk and the observed surface brightness at the break point. This correlation should appear only close to the edge-on view and is due to projection effects, without reflecting a real correlation of intrinsic galactic properties. Figure 12 demonstrates this effect: its left panel shows the r-band surface brightness at the break point as a function of the radial-scale length of the outer disk (normalized to the radius of the 27th-magnitude isophote for consistency). Indeed, there is a rather strong correlation (Pearson's correlation coefficient is -0.444): galaxies with a more extended outer disk have higher break point surface brightness. The right panel of this figure shows the same parameters recomputed to the face-on orientation. In this case, the correlation coefficient drops significantly (to -0.260).

This means that the observed correlation is a result of projection effects and that one must be careful when analyzing correlations between decomposition parameters for galaxies with different orientations.

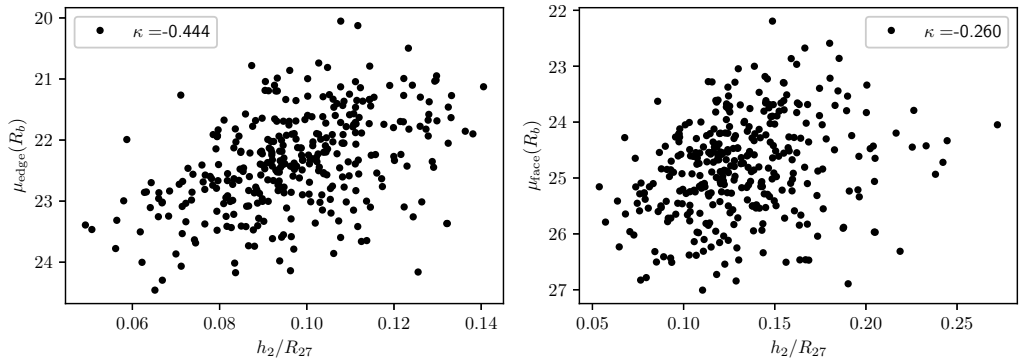

Figure 12. Radial exponential-scale length of an outer disk (normalized by the 27th magnitude isophote radius) vs. surface brightness at the break point (all values in r-band). (**Left-panel**): observed values, (**right panel**): recalculated to the face-on orientation.

5.3. Two Kinds of Downbending Breaks

Figure 13 shows how the surface brightness at the break point (recomputed to the face-on orientation) and the disk color at the break point depend on the break strength. One thing that is readily seen from this figure is that there are two distinct sets of points: very strong Type II breaks (with the strength values < -2.0, marked as red dots) and rather mild Type II breaks (with the strength values $\gtrsim -1.5$, marked as blue dots). There are almost no breaks between these two groups.

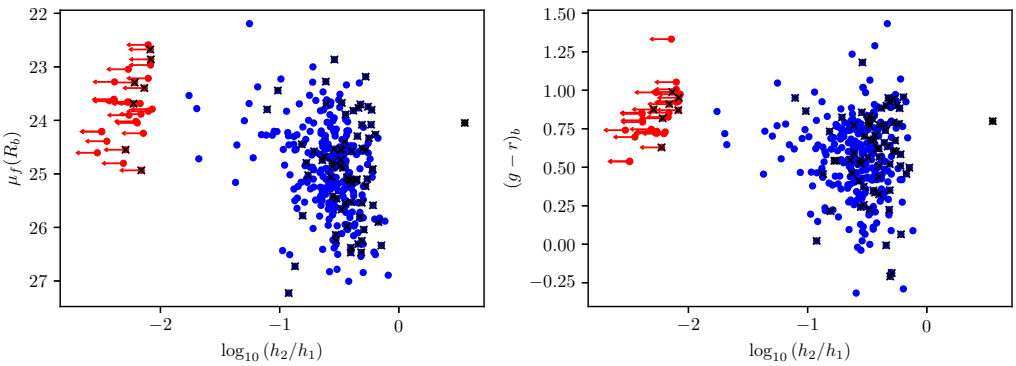

Figure 13. (**Left panel**): face-on surface brightness for break point vs. break strength. (**Right panel**): $(g-r)$ color for break point vs. break strength. Red dots mark disks with strength < -2.0, and blue dots mark those with strength > -2.0. The black dot is a sole galaxy with a Type III break (PGC 731, see Appendix C for details about this object). Crosses mark galaxies that host apparent X-structures.

In all cases, the very high negative values of the break strength parameter are due to large radial-scale lengths of the inner disk. Figure 14 demonstrates examples of three such galaxies. It is remarkable how the true break locations (shown by x-marks in the figure) differ from the apparent ones due to projection effects (see Figure 2 and the related discussion in text). Some disks exhibit an almost flat light distribution in their inner regions, so very high values of h_1 are required to fit it. Interestingly, studies of face-on and mildly inclined galaxies usually do not demonstrate galaxies with such high break strengths. For example in [40] the strongest downbending break has $s \approx -0.8$, while in [77] the most extreme Type II break has a strength of about -1 (such galaxies are dubbed "flat inner disks" in that work). However, the works that focus on edge-on galaxies do show some galaxies with very strong breaks in their samples, although the number of articles with

large samples of edge-on galaxies is low. For example, in [78] in a sample of 70 edge-on galaxies there is a galaxy with $s = -1.4$ (ESO 469-015). In [79] the decomposition of a sample of 71 edge-on galaxies is performed, and the authors note that for some of them the radial-scale length of the inner disk reaches such high values that the light distribution in the inner regions can be effectively considered flat. We note here that in this case the model degenerates in the h_1 value: if $h_1 \gg r_b$, the surface brightness of the inner disk becomes almost flat, and further increasing the h_1 value does not lead to significant changes in the model, and therefore in the obtained χ^2 value. This means that the true values of h_1 and s become undefined in such models. To emphasize this, we marked strong breaks as upper limits in Figure 13. One should treat these values carefully, and only use them as an indicator of a strong break in the galaxy.

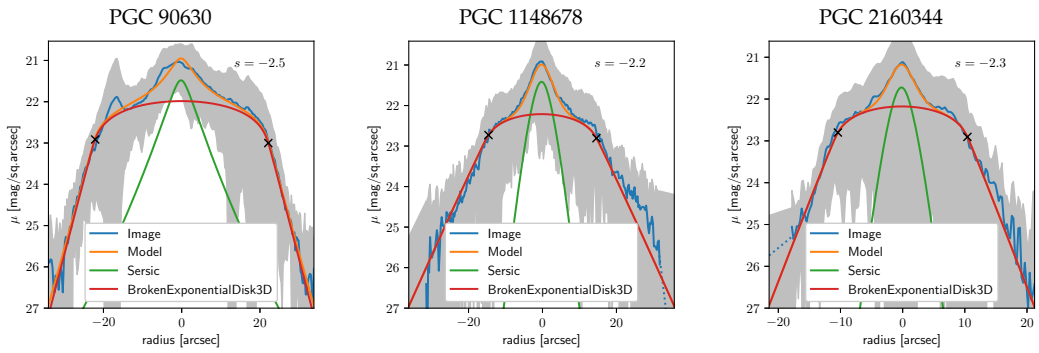

Figure 14. Decomposition results for three galaxies with very strong breaks. All markings are the same as in Figure 4.

One possible explanation for a flat inner disk is the presence of an additional component such as an outer ring (see [77]), which adds extra light that, when combined with an exponential disk, may result in an almost flat light distribution. Another possibility is a strong bar which can either manifest itself as an additional component, or form a ring at the outer Lindblad resonance (OLR) which leads to an apparent Type II break [24]. In the face-on orientation, such components would be easily detectable, but in the edge-on view their identification is more complicated due to projection effects. Another possibility is strong dust attenuation that absorbs the light from central regions. To check for clues, we examine 2D plots of original images, models and residuals for some galaxies with strong breaks in Figure 15, with break locations marked. It can be seen from these images that there are no obvious structures located near the break radii that could cause a flat inner disk appearance. Even the residual maps, which usually highlight substructures that are not accounted for by the model, do not show anything significant near or inside the break locations. In particular, we do not see the presence of X-structures in the residual maps, features that are manifestations of a bar's presence in the edge-on orientation [80,81]. A strong bar could result in a density depression in the inner disk regions and even lead to disks with central holes (so-called antitruncated disks) [65]. We checked residual maps of all galaxies for the presence of X-structures using [82], and found that the number of galaxies that host X-structures is 69 out of 311 galaxies (22%) and 7 out of 30 galaxies (23%) for weak and strong breaks respectively, so the presence of bars/X-structures alone cannot explain a strong break. It can also be seen that these galaxies are not exceptionally dusty ones (at least, the dust lanes are not prominent in the optical images).

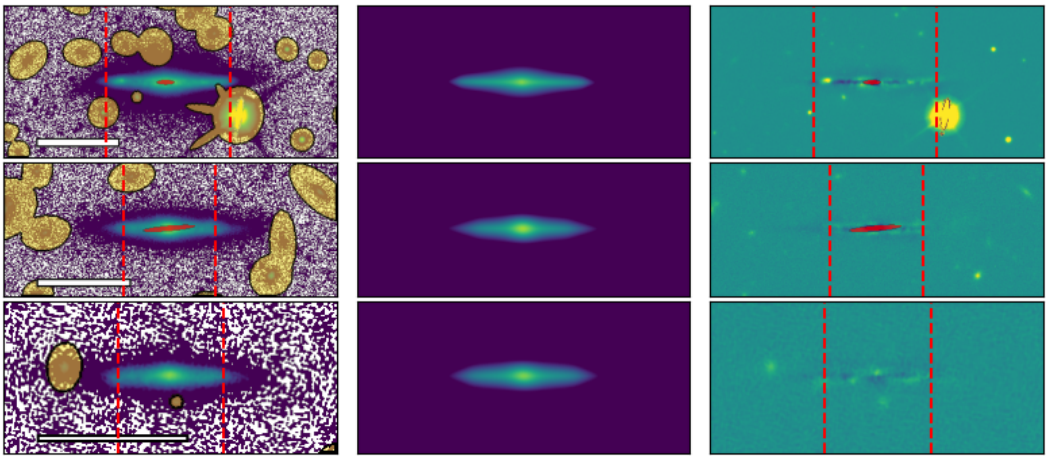

Figure 15. Decomposition results for the same three galaxies as in Figure 14, shown as 2D image maps. All markings are the same as in Figure 5, with one exception: vertical dashed red lines indicate break locations.

As a final note, we would like to point out that from the radial slices alone (Figure 14) it may appear that there is a degeneracy between the bulge and the inner disk: if the bulge becomes fainter, the inner disk will become steeper to compensate for it, and this will resolve the flat inner disk problem. However, since we employ the two-dimensional decomposition, this is not the case. If we reduced the bulge brightness, this would be readily noticeable in the 2D residual maps as two bright regions above and below the disk center, where the bulge light is underestimated and where the disk could not account for it. There is no difference between the mean bulge-to-total ratios between galaxies with strong and weak breaks (0.23 ± 0.11 and 0.22 ± 0.13 in the *r*-band respectively), whereas in the case where the bulge becomes larger to account for some disk light and produce a flat disk appearance, we would expect a systematic difference between the two subsamples. There is also no difference in the ratio of bulge effective radius to disk vertical scale (2.67 ± 1.17 and 2.50 ± 1.48 in the *r*-band accordingly), so we rule out the possibility that galaxies with strong breaks host geometrically smaller bulges that would make it easier for them to blend in with the disks. We also do not find a significant difference in the mean stellar mass between galaxies hosting weak and strong breaks ($\log(M_*/M_\odot) = 10.52 \pm 0.46$ and 10.54 ± 0.36).

To investigate the possibility of degeneracy between the bulge parameters and the inner disk scale we performed the following experiment: For a PGC 2160344 galaxy (a strong break without prominent X-structure) we ran a set of decompositions where we forced the bulge to converge to brighter/fainter bulge-to-total ratios than those of the best fit. It is natural to expect that if we force the bulge to have a lower bulge-to-total ratio, the inner disk scale will become larger to compensate for the missing bulge light. The question is whether this results in the same quality fit (i.e., whether there is true degeneracy between bulge parameters and the h_1 value). Figure 16 demonstrates the results of such an experiment. On the left panel we show photometric cuts taken from an "image-model" residual map parallel to the disk plane outside the dust lane (only central regions inside the break radius are shown). The black solid line shows the result for a best-fit decomposition with free bulge parameters. Dotted lines show residuals of decompositions where we forced the bulge to have larger B/T ratios, and dot-dashed lines show residuals where we forced the bulge to have lower B/T ratios. It is clear from this plot that models with both brighter and fainter bulges demonstrate larger residuals. The same result but in terms of χ^2 values is shown in the middle panel of the same figure. Here the blue star shows the best-fitting χ^2 value, and red dots show results with fainter/brighter

bulges, all of which have larger χ^2. The right panel shows the break strength value as a function of the fixed bulge-to-total value. It is clear that if we force the bulge to have a lower value, we can obtain a significantly lower break strength, but at the cost of a worse fit. The Bayesian information criterion (BIC) value of the best fit is 28,721 compared to 31,224 for the one with a fainter bulge but lower break strength (the one with $h_2/h_1 \approx -1$ in the figure), which makes the best fit with a free bulge the preferable one.

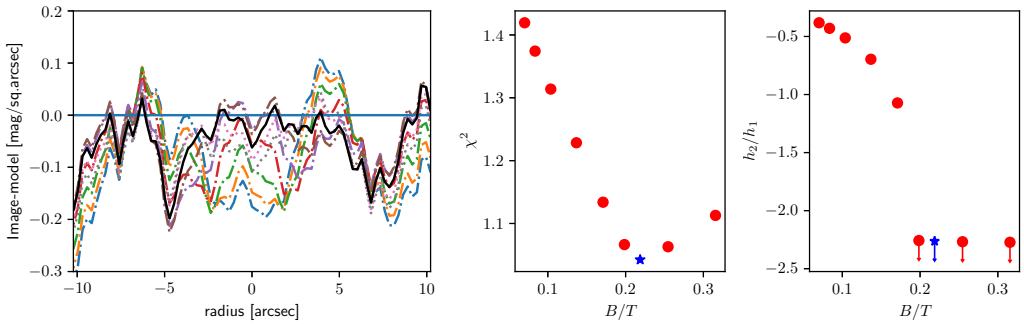

Figure 16. Results of a test for the degeneracy between bulge parameters and the break strength (see text). (**Left panel**): photometric cuts along the disk plane in the "image-model" residual map for a set of decompositions with different values of bulge-to-total ratio. The solid black line shows the results of the best decomposition, dotted lines represent B/T fixed to larger values, and dot-dashed lines represent B/T fixed to lower values. (**Middle** and **right panels**)—χ^2 and break strength values as a function of B/T value, with blue stars showing optimal decomposition with free bulge parameters.

A possible solution to this problem could be obtained by performing the decomposition of highly inclined—but not edge-on—galaxies, where the dust impact, bulge-disk degeneracy and projection effects are lower.

5.4. Disk Color vs. Break Strength

Since we performed photometric decomposition of the galaxy images, we obtained fluxes for individual components (bulge and disk) separately. Performing the decomposition in different passbands allows us to obtain the colors of these components. To do so, we converted the integrated fluxes of the components into magnitudes and accounted for the Galactic dust extinction in all photometric bands, with calculations performed following recalibrated SFD dust maps [66] (the corrections were calculated from $E(B-V)$ reddening for $R_V = 3.1$ using coefficients from their Table 6).

Figure 17 shows the relation between the integrated disk $(g-r)$ color and the break strength. As in the previous subsection, we divided all the breaks into two subsamples: strong ones (with break strength < -2) and weak ones (with strength > -2). As can be seen from the figure, both groups of breaks exhibit significant correlations. For weak breaks, Pearson's correlation coefficient is 0.337 (p-value $1.06 \cdot 10^{-9}$), while for strong breaks, the correlation coefficient is 0.539 (p-value 0.002). We performed linear regression on the data points of both break groups and obtained the following results: for weak breaks $s = 0.828 \cdot (g-r)_{\rm disk} - 1.228$, and for strong breaks $s = 0.705 \cdot (g-r)_{\rm disk} - 2.747$. It is notable that two such distinct groups of breaks follow a "color–strength" relation with very similar slopes. We also note, that disks with strong breaks are on average somewhat bluer than disks with weak breaks, but their color ranges overlap greatly, so it is impossible to distinguish two types of disks based on color alone.

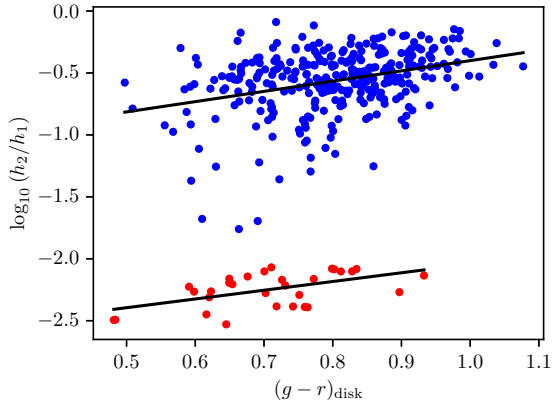

Figure 17. Break strength in the r-band vs. disk $(g-r)$ color. Blue dots: weak breaks (strength > -2), red dots: strong breaks (strength < -2). Solid black lines: linear regressions for the two break groups.

The interpretation of this correlation between the disk color and the break strength can be made within the framework of models that invoke star-formation to explain the generation of breaks. Bluer disks should host more intense current or recent star-formation and therefore should be more prone to forming prominent breaks. As mentioned in the Introduction, many studies demonstrate, that breaks are observed more frequently in galaxies of later Hubble types, where star-formation is higher [10,24–28], whereas when a galactic star-formation is suppressed, for example, by ram pressure stripping, the number of breaks decreases [29–31,34,35]. The correlation we report here is therefore in line with these findings.

5.5. Break Strength as a Function of Wavelength

In [39] on a small sample of face-on to intermediately inclined galaxies from SDSS Stripe 82 [83], it was demonstrated that the strength of Type II breaks decreases, on average, with increasing wavelength in the optical bands from u to z. This result was confirmed by [26] using a larger sample of mildly inclined galaxies from the S^{4}G sample [84]: u-band breaks turned out to be stronger than those measured in the infrared spectrum.

Here we test this result for a sample of edge-on galaxies. Figure 18 shows the distribution of differences between break strengths measured in the g- and i-bands. Since the footprint of the DESI Legacy survey in the i-band is smaller than that in the g-band, only 165 galaxies in our sample have images in both bands. In this figure we also exclude the sole upbending galaxy in our sample, so only Type II galaxies are presented; thus, lower values of $s(g) - s(i)$ indicate stronger breaks in the g-band that in the i-band. As can be seen from the figure, all galaxies show negative values of $s(g) - s(i)$, meaning they have stronger breaks at bluer wavelengths. This confirms the result from [26,39] obtained with a different method and for a different sample of galaxies.

As in [26], we found that the main source of the dependence of break strength on wavelength is related to the changes in the inner disk radial scale rather than the outer one. We computed the normalized average differences between the radial scales of inner and outer disks in the g- and i-bands as

$$\Delta h_i = \frac{h(g) - h(i)}{h(g)}, \quad i = 1, 2,$$

and found that $\Delta h_1 = 0.44 \pm 0.27$, while $\Delta h_2 = 0.03 \pm 0.13$. All inner disks have larger radial scales in the g-band than in the i-band. The differences in radial scales for the outer disks are distributed around zero with considerably lower scatter. If the break is caused by a drop in star-formation and the outer disk is populated by radial migration of stars,

we should observe larger radial scales of outer disks at longer wavelengths, since older stellar populations have had more time to move outward. The same systematic behavior should be observed if a break appears as a result of a local enhancement in sSFR both inside and outside the break radius, as was seen in simulations by [36]. In this work, we do not observe a statistically significant dependence of the outer disk scale on the wavelength.

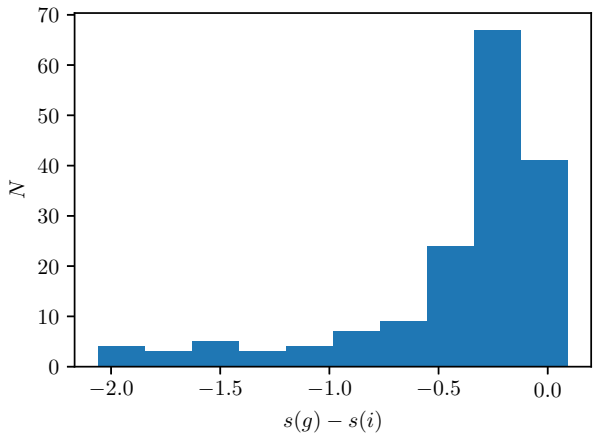

Figure 18. Distribution if differences between breaks strengths measured in g and i-bands. For Type II breaks, lower values mean stronger breaks in the g-band.

We should mention that although we attempted to reduce the influence of dust on the decomposition results by masking dusty regions, non-planar dust can still affect the measured parameters as a function of wavelength. For more robust results, decomposition of a comparably sized sample using a radiative transfer approach is needed to account for the dust more carefully. However, such an analysis is yet to be done.

5.6. Rotation Velocity

Although galaxies in our sample are relatively close, only a minority of them (100 objects) have maximal rotation velocity estimates in the HyperLEDA database [85]. Stellar masses derived from our photometry measurements obtained from decomposition models correlate well with $V_{\max}$ (Pearson's correlation 0.781, p-value $3{\cdot}10^{-22}$).

We found that there is a significant correlation between the break radius expressed in absolute units and the maximum of the rotation velocity. Pearson's correlation coefficient is 0.511, and the p-value is $1.7{\cdot}10^{-7}$ (see Figure 19, left panel). The correlation between the break radius and the rotation velocity was studied in several articles because some theories associate breaks with maximum angular momentum in disks. It seems that when the break radius is expressed in relative units, the correlation is weak or absent. In [24,86] the break radius was expressed in terms of inner disk radial scales and did not show a significant correlation with rotation velocity. In [25], where the correlation was found, the break was expressed in units of R_{25}. In [41] a strong correlation between R_b and $V_{\max}$ was found if the break radius is expressed in absolute units. We confirm these findings: according to our data there is a significant correlation if R_b is expressed in parsecs, whereas if we normalize it by R_{27}, the correlation disappears. Since the stellar mass derived from decomposition correlates well with the break radius, but is measured for a larger sample of galaxies, we also plot in Figure 19 (right panel) the correlation between the stellar mass and R_b. These two parameters also show significant correlation with Pearson's coefficient of 0.705, which was also demonstrated previously in [26].

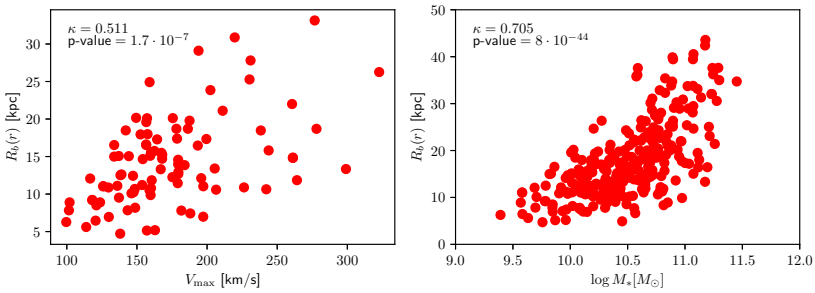

Figure 19. Break radius in *r*-band (**left**) and stellar mass (**right**) vs. maximum rotation velocity.

6. Conclusions

In this work, we performed two-dimensional photometric decomposition of a sample of 375 disk galaxies viewed in the edge-on orientation. To perform the decomposition, we utilized *g*-, *r*- and *i*-band images from the DESI Legacy DR10 survey, which is considerably more in-depth than many older wide-field surveys—a factor crucial for this task. Our main results are summarized below.

(i) The vast majority of disks in our sample have Type II (downbending) breaks: such a feature is found in 341 galaxies ($90.9 \pm 9.5\%$). The fractions of Type II galaxies in most previous works are considerably lower ($\sim$50%) and do not fall into the error margins specified here, so the difference is significant. Only one galaxy in our sample has a Type III (upbending) break, while the remaining 33 galaxies ($8.8 \pm 3.0\%$) are well described by a single exponential profile (Type I).

(ii) Such a high fraction of Type II breaks can be attributed to greater photometric depth of the images used compared to older wide-field surveys employed in many previous studies on the topic, and to projection effects that make edge-on galaxies more favorable for break detection.

(iii) The same projection effects can lead to artificial correlations between some decomposition parameters, which disappear when these parameters are recalculated to a face-on orientation.

(iv) Some galaxies exhibit remarkably strong breaks with an inner-to-outer radial-scale ratio greater than 100. In all cases, such a high ratio is due to a very large radial scale of the inner disk, which produces an almost flat light distribution in the central regions.

(v) Such strong breaks are separated from normal ones in some parameter planes, such as "break strength vs. break color" and "break strength vs. break surface brightness", with almost no intermediate breaks between the two groups.

Based on these results, we conclude that Type II disk breaks are almost ubiquitous in disks, at least in ones that have the same mass and Hubble type distribution as in our sample. With a new generation of wide-field surveys that will be 2–3 magnitudes deeper than current ones, many Type I galaxies would reveal breaks in their outer regions that are currently beyond the detection limit.

The main question arising from this work concerns the nature of strong breaks. They appear to be absent in samples of face-on or moderately inclined galaxies (or at least their fraction is considerably lower), so projection effects may play a role, especially in combination with dust attenuation. In this work we attempted to mitigate the impact of dust on decomposition by masking the dust lane, but some off-plane dust may still influence the appearance of the radial profile. Still, the visual inspection of galaxies with strong breaks does not suggest that such galaxies contain very prominent dust lanes, and the colors of their disks are not redder than those with moderate breaks. The visual inspection of residual maps also does not reveal that some additional components exist in such galaxies, which may enhance the observed break strength.

A possible way to address this problem is to perform decomposition of a sample of highly inclined—but not edge-on—galaxies. Dependence of the strong-break fraction on the inclination in such a sample could shed light on the impact of the projection effects on strong-break generation. This, however, would be a difficult task since the decomposition of such galaxies faces the complication of unknown disk inclination. For edge-on galaxies, the inclination can be fixed to 90 degrees, while for moderately inclined ones the vertical structure of galaxies plays a less important role and they can be adequately explained by a two-dimensional (zero-depth) exponential. Galaxies with an almost edge-on inclination should be treated differently from face-on and perfect edge-on cases, because one can neglect neither their thickness nor their deviation from a perfect edge-on orientation. The sample discussed in this work does not contain such galaxies, and we leave their investigation for future work.

Supplementary Materials: The following supporting information can be downloaded at https://www.mdpi.com/article/10.3390/galaxies14040067/s1, Table S1: Decomposition parameters of our sample of galaxies.

Author Contributions: Conceptualization, S.S.S., I.V.C. and A.A.M.; methodology, S.S.S., I.V.C. and A.A.M.; software, S.S.S. and I.V.C.; validation, V.P.R., M.D.K. and A.M.S.; formal analysis, S.S.S., I.V.C. and A.A.M.; investigation, S.S.S., I.V.C., A.A.M., V.P.R., M.D.K., D.I.M., A.V.A. and A.M.S.; resources, S.S.S. and A.A.M.; data curation, S.S.S., I.V.C. and A.A.M.; writing—original draft preparation, S.S.S., I.V.C. and A.A.M.; writing—review and editing, V.P.R., M.D.K., D.I.M., A.V.A. and A.M.S.; visualization, S.S.S. and I.V.C.; supervision, V.P.R.; project administration, A.A.M.; funding acquisition, A.A.M. All authors have read and agreed to the published version of the manuscript.

Funding: This research was supported by the Russian Science Foundation grant № 24–72–10084.

Data Availability Statement: The decomposition results for the galaxy sample are availabe as Supplementary Materials.

Acknowledgments: We thank the anonymous reviewers for their valuable comments and constructive suggestions, which significantly helped improve the quality of our manuscript. This research has made use of the NASA/IPAC Extragalactic Database (NED), which is operated by the Jet Propulsion Laboratory, California Institute of Technology, under contract with the National Aeronautics and Space Administration. This research has made use of the DESI Legacy Survey. The Legacy Surveys consist of three individual and complementary projects: the Dark Energy Camera Legacy Survey (DECaLS; Proposal ID #2014B-0404; PIs: David Schlegel and Arjun Dey), the Beijing–Arizona Sky Survey (BASS; NOAO Prop. ID #2015A-0801; PIs: Zhou Xu and Xiaohui Fan), and the Mayall z-band Legacy Survey (MzLS; Prop. ID #2016A-0453; PI: Arjun Dey). DECaLS, BASS and MzLS together include data obtained, respectively, at the Blanco telescope, Cerro Tololo Inter-American Observatory, NSF's NOIRLab; the Bok telescope, Steward Observatory, University of Arizona; and the Mayall telescope, Kitt Peak National Observatory, NOIRLab. Pipeline processing and analyses of the data were supported by NOIRLab and the Lawrence Berkeley National Laboratory (LBNL). The Legacy Surveys project is honored to be permitted to conduct astronomical research on Iolkam Du'ag (Kitt Peak), a mountain with particular significance to the Tohono O'odham Nation. NOIRLab is operated by the Association of Universities for Research in Astronomy (AURA) under a cooperative agreement with the National Science Foundation. LBNL is managed by the Regents of the University of California under contract to the U.S. Department of Energy. This project used data obtained with the Dark Energy Camera (DECam), which was constructed by the Dark Energy Survey (DES) collaboration. Funding for the DES Projects has been provided by the U.S. Department of Energy; the U.S. National Science Foundation; the Ministry of Science and Education of Spain; the Science and Technology Facilities Council of the United Kingdom; the Higher Education Funding Council for England; the National Center for Supercomputing Applications at the University of Illinois at Urbana-Champaign; the Kavli Institute of Cosmological Physics at the University of Chicago; the Center for Cosmology and Astro-Particle Physics at Ohio State University; the Mitchell Institute

for Fundamental Physics and Astronomy at Texas A&M University; Financiadora de Estudos e Projetos; Fundacao Carlos Chagas Filho de Amparo; Financiadora de Estudos e Projetos; Fundacao Carlos Chagas Filho de Amparo a Pesquisa do Estado do Rio de Janeiro; Conselho Nacional de Desenvolvimento Cientifico e Tecnologico and the Ministerio da Ciencia; Tecnologia e Inovacao; the Deutsche Forschungsgemeinschaft; and the Collaborating Institutions of the Dark Energy Survey. The Collaborating Institutions are Argonne National Laboratory, the University of California at Santa Cruz, the University of Cambridge, Centro de Investigaciones Energeticas, Medioambientales y Tecnologicas-Madrid, the University of Chicago, University College London, the DES-Brazil Consortium, the University of Edinburgh, the Eidgenossische Technische Hochschule (ETH) Zurich, the Fermi National Accelerator Laboratory, the University of Illinois at Urbana-Champaign, the Institut de Ciencies de l'Espai (IEEC/CSIC), the Institut de Fisica d'Altes Energies, the Lawrence Berkeley National Laboratory, the Ludwig Maximilians Universitat Munchen and the associated Excellence Cluster Universe, the University of Michigan, NSF's NOIRLab, the University of Nottingham, Ohio State University, the University of Pennsylvania, the University of Portsmouth, the SLAC National Accelerator Laboratory, Stanford University, the University of Sussex, and Texas A&M University. BASS is a key project of the Telescope Access Program (TAP), which has been funded by the National Astronomical Observatories of China, the Chinese Academy of Sciences (the Strategic Priority Research Program "The Emergence of Cosmological Structures", Grant #XDB09000000), and the Special Fund for Astronomy from the Ministry of Finance. The BASS is also supported by the External Cooperation Program of the Chinese Academy of Sciences (Grant #114A11KYSB20160057), and the Chinese National Natural Science Foundation (Grant #12120101003, #11433005). The Legacy Survey team makes use of data products from the Near-Earth Object Wide-field Infrared Survey Explorer (NEOWISE), which is a project of the Jet Propulsion Laboratory/California Institute of Technology. NEOWISE is funded by the National Aeronautics and Space Administration. The Legacy Surveys imaging of the DESI footprint is supported by the Director, Office of Science, Office of High Energy Physics of the U.S. Department of Energy under Contract No. DE-AC02-05CH1123; by the National Energy Research Scientific Computing Center, a DOE Office of Science User Facilities under the same contract; and by the U.S. National Science Foundation, Division of Astronomical Sciences, under Contract No. AST-0950945 to NOAO.

Conflicts of Interest: The authors declare no conflicts of interest.

Appendix A. Flaring Strength as a Function of Break Strength

In this section we present the derivation of Equation (8), which describes the functional form of flaring that is required to produce an exponential break of a given strength α. Let us consider the volume brightness density of a broken exponential disk beyond the break radius:

$$\rho_{\text{broken}}(x,z) = \rho(R_b)\exp\left(-\frac{x}{h_2}\right)\exp\left(-\frac{|z|}{h_z}\right),$$

where x is the distance from the break point, and $\rho(R_b)$ is the volume density at the break point. The volume brightness density of a flaring disk in the same region would be

$$\rho_{\text{flaring}}(x,z) = \rho(R_f)\exp\left(-\frac{x}{h_1}\right)\exp\left(-\frac{|z|}{h_z(x)}\right)\frac{h_{z,0}}{h_z(x)},$$

where R_f is the radius of flaring onset (by construction $R_f = R_b$), $h_{z,0}$ is the height of the unflared disk, and $h_z(x)$ is a function that describes how the vertical scale depends on radius, i.e., the desired flaring function.

Since we are interested in the impact of flaring on producing the light depletion in the disk plane, we can rewrite the same equations for zero height:

$$\rho_{\text{broken}}(x) = \rho(R_b)\exp\left(-\frac{x}{h_2}\right),$$

and

$$\rho_{\text{flaring}}(x) = \rho(R_f)\exp\left(-\frac{x}{h_1}\right)\frac{h_{z,0}}{h_z(x)}.$$

By construction, these two equations describe the same observed light distribution, so we can equate them:

$$\rho(R_b)\exp\left(-\frac{x}{h_2}\right) = \rho(R_f)\exp\left(-\frac{x}{h_1}\right)\frac{h_{z,0}}{h_z(x)}.$$

Since $\rho(R_b) = \rho(R_f)$ and $h_2 = \alpha h_1$ we can rewrite this equation as

$$\exp\left(-\frac{x}{\alpha h_1}\right) = \exp\left(-\frac{x}{h_1}\right)\frac{h_{z,0}}{h_z(x)},$$

from which $h_z(x)$ can be inferred as

$$h_z(x) = \exp\left(\frac{1-\alpha}{\alpha}\right)h_z(R_b).$$

Appendix B. Break Point Surface Brightness in Edge-On and Face-On Orientations

In Section 2 we showed an equation that allows one to compare the surface brightness of a disk at its break point in edge-on and face-on orientations (Equation (6)), and demonstrated the result of this equation for the specific combination of disk parameters ($h_2 = 0.25h_1$, $R_b = 4h_1$, and $h_z = 0.2h_1$). Here we show the difference between face-on and edge-on surface brightnesses for a range of disk parameters to demonstrate the expected strength of the effect. Figure A1 shows the results of computations for a range of h_2 from 0.1 to 0.8 and a range of R_b from 3.0 to 6.0 (in units of h_1).

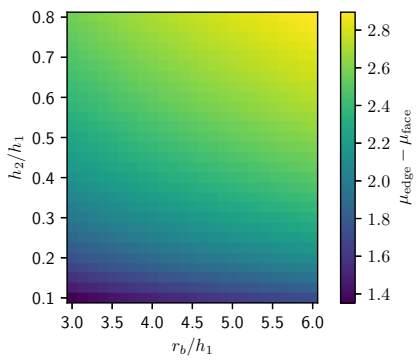

Figure A1. Difference between surface brightness in face-on and edge-on orientations (in magnitudes) as a function of h_2 and R_b.

Appendix C. The Case of PGC 731

In this appendix section we present the case of PGC 731, the sole galaxy of our sample that was fitted with an upbending disk profile. Figure A2 shows decomposition results as 2D maps (top panels) and as a slice along a disk plane (bottom panel). The break location is shown by vertical dashed lines. As can be seen from the figure, the profile indeed demonstrates a break, although it is located in the inner regions of the galaxy, at a radius about two times larger than the extent of the prominent X-structure. This may indicate that the presence of a bar/X-structure alters the inner shape of the disk component, and the upbending nature of this galaxy is questionable.

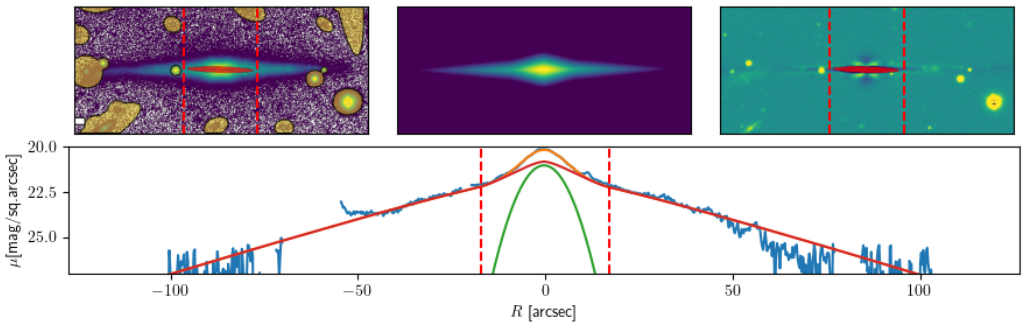

Figure A2. Decomposition results for PGC 731. (**Top**): 2D maps as in Figure 5; (**bottom**): radial slice as in Figure 4. Vertical dashed lines show break locations.

References

1. Conselice, C.J. The fundamental properties of galaxies and a new galaxy classification system. *Mon. Not. R. Astron. Soc.* **2006**, *373*, 1389–1408. [CrossRef]
2. Kelvin, L.S.; Driver, S.P.; Robotham, A.S.G.; Graham, A.W.; Phillipps, S.; Agius, N.K.; Alpaslan, M.; Baldry, I.; Bamford, S.P.; Bland-Hawthorn, J.; et al. Galaxy And Mass Assembly (GAMA): UgrizYJHK Sérsic luminosity functions and the cosmic spectral energy distribution by Hubble type. *Mon. Not. R. Astron. Soc.* **2014**, *439*, 1245–1269. [CrossRef]
3. Peng, C.Y.; Ho, L.C.; Impey, C.D.; Rix, H.W. Detailed Decomposition of Galaxy Images. II. Beyond Axisymmetric Models. *Astron. J.* **2010**, *139*, 2097–2129. [CrossRef]
4. Erwin, P. IMFIT: A Fast, Flexible New Program for Astronomical Image Fitting. *Astrophys. J.* **2015**, *799*, 226. [CrossRef]
5. Sérsic, J.L. Influence of the atmospheric and instrumental dispersion on the brightness distribution in a galaxy. *Boletín Asoc. Argent. Astron.* **1963**, *6*, 41–43.
6. Patterson, F.S. The Luminosity Gradient of Messier 33. *Harv. Coll. Obs. Bull.* **1940**, *914*, 9–10.
7. de Vaucouleurs, G. Photoelectric Photometry of Messier 33 IN the u, b, v, System. *Astrophys. J.* **1959**, *130*, 728. [CrossRef] [PubMed]
8. Freeman, K.C. On the Disks of Spiral and S0 Galaxies. *Astrophys. J.* **1970**, *160*, 811. [CrossRef] [PubMed]
9. van der Kruit, P.C. Optical surface photometry of eight spiral galaxies studied in Westerbork. *Astron. Astrophys. Suppl. Ser.* **1979**, *38*, 15–38.
10. Erwin, P.; Pohlen, M.; Beckman, J.E. The Outer Disks of Early-Type Galaxies. I. Surface-Brightness Profiles of Barred Galaxies. *Astron. J.* **2008**, *135*, 20–54. [CrossRef]
11. Sil'chenko, O.K. Exponential bulges and antitruncated disks in lenticular galaxies. In *Proceedings of the Galaxy Disk in Cosmological Context, IAU Symposium*; Andersen, J., Nordströara, M.B., Bland-Hawthorn, J., Eds.; Cambridge University Press: Cambridge, UK, 2009; Volume 254, pp. 173–178. [CrossRef]
12. Mestel, L. On the galactic law of rotation. *Mon. Not. R. Astron. Soc.* **1963**, *126*, 553. [CrossRef]
13. Sellwood, J.A.; Binney, J.J. Radial mixing in galactic discs. *Mon. Not. R. Astron. Soc.* **2002**, *336*, 785–796. [CrossRef]
14. Roškar, R.; Debattista, V.P.; Stinson, G.S.; Quinn, T.R.; Kaufmann, T.; Wadsley, J. Beyond Inside-Out Growth: Formation and Evolution of Disk Outskirts. *Astrophys. J.* **2008**, *675*, L65. [CrossRef]
15. Sellwood, J.A. Galaxy models with live halos. *Astron. Astrophys.* **1980**, *89*, 296–307.
16. Athanassoula, L. Angular Momentum Redistribution and the Evolution and Morphology of Bars. In *Galaxies and Chaos*; Contopoulos, G., Voglis, N., Eds.; Springer: Berlin/Heidelberg, Germany, 2003; Volume 626, pp. 313–326. [CrossRef]
17. Debattista, V.P.; Mayer, L.; Carollo, C.M.; Moore, B.; Wadsley, J.; Quinn, T. The Secular Evolution of Disk Structural Parameters. *Astrophys. J.* **2006**, *645*, 209–227. [CrossRef]
18. Muñoz-Mateos, J.C.; Sheth, K.; Gil de Paz, A.; Meidt, S.; Athanassoula, E.; Bosma, A.; Comerón, S.; Elmegreen, D.M.; Elmegreen, B.G.; Erroz-Ferrer, S.; et al. The Impact of Bars on Disk Breaks as Probed by S^4G Imaging. *Astrophys. J.* **2013**, *771*, 59. [CrossRef]
19. Goldreich, P.; Lynden-Bell, D.I. Gravitational stability of uniformly rotating disks. *Mon. Not. R. Astron. Soc.* **1965**, *130*, 97. [CrossRef]
20. Kennicutt, R.C., Jr. The Star Formation Law in Galactic Disks. *Astrophys. J.* **1989**, *344*, 685. [CrossRef] [PubMed]
21. Bakos, J.; Trujillo, I.; Pohlen, M. Color Profiles of Spiral Galaxies: Clues on Outer-Disk Formation Scenarios. *Astrophys. J.* **2008**, *683*, L103. [CrossRef] [PubMed]
22. Chamba, N.; Trujillo, I.; Knapen, J.H. The edges of galaxies: Tracing the limits of star formation. *Astron. Astrophys.* **2022**, *667*, A87. [CrossRef]

23. Raji, S.; Trujillo, I.; Buitrago, F.; Golini, G.; Cejudo, I.R. Revisiting the structure of galactic disks with deep imaging. *Astron. Astrophys.* **2025**, *704*, A335. [CrossRef]
24. Pohlen, M.; Trujillo, I. The structure of galactic disks. Studying late-type spiral galaxies using SDSS. *Astron. Astrophys.* **2006**, *454*, 759–772. [CrossRef]
25. Gutiérrez, L.; Erwin, P.; Aladro, R.; Beckman, J.E. The Outer Disks of Early-type Galaxies. II. Surface-brightness Profiles of Unbarred Galaxies and Trends with Hubble Type. *Astron. J.* **2011**, *142*, 145. [CrossRef]
26. Laine, J.; Laurikainen, E.; Salo, H. Influence of galaxy stellar mass and observed wavelength on disc breaks in S^4G, NIRS0S, and SDSS data. *Astron. Astrophys.* **2016**, *596*, A25. [CrossRef]
27. Méndez-Abreu, J.; Ruiz-Lara, T.; Sánchez-Menguiano, L.; de Lorenzo-Cáceres, A.; Costantin, L.; Catalán-Torrecilla, C.; Florido, E.; Aguerri, J.A.L.; Bland-Hawthorn, J.; Corsini, E.M.; et al. Two-dimensional multi-component photometric decomposition of CALIFA galaxies. *Astron. Astrophys.* **2017**, *598*, A32. [CrossRef]
28. Tang, Y.; Chen, Q.; Zhang, H.X.; Lin, Z.; Chen, G.; Gao, Y.; Liang, Z.; Liu, H.; Kong, X. New Constraints on the Origin of Surface Brightness Profile Breaks of Disk Galaxies from MaNGA. *Astrophys. J.* **2020**, *897*, 79. [CrossRef]
29. Erwin, P.; Gutiérrez, L.; Beckman, J.E. A Strong Dichotomy in S0 Disk Profiles between the Virgo Cluster and the Field. *Astrophys. J.* **2012**, *744*, L11. [CrossRef]
30. Head, J.T.C.G.; Lucey, J.R.; Hudson, M.J. Beyond Sérsic + exponential disc morphologies in the Coma Cluster. *Mon. Not. R. Astron. Soc.* **2015**, *453*, 3729–3753. [CrossRef]
31. Pranger, F.; Trujillo, I.; Kelvin, L.S.; Cebrián, M. The effect of environment on the structure of disc galaxies. *Mon. Not. R. Astron. Soc.* **2017**, *467*, 2127–2144. [CrossRef]
32. Sil'chenko, O.K.; Kniazev, A.Y.; Chudakova, E.M. The Structure of Large-scale Stellar Disks in Cluster Lenticular Galaxies. *Astron. J.* **2018**, *156*, 118. [CrossRef]
33. Sil'chenko, O.K.; Kniazev, A.Y.; Chudakova, E.M. The Structure of Stellar Disks in Isolated Lenticular Galaxies. *Astron. J.* **2020**, *160*, 95. [CrossRef]
34. Pfeffer, J.L.; Bekki, K.; Forbes, D.A.; Couch, W.J.; Koribalski, B.S. Using the EAGLE simulations to elucidate the origin of disc surface brightness profile breaks as a function of mass and environment. *Mon. Not. R. Astron. Soc.* **2022**, *509*, 261–271. [CrossRef]
35. Mondelin, M.; Bournaud, F.; Cuillandre, J.C.; Codis, S.; Stone, C.; Bolzonella, M.; Sorce, J.G.; Kluge, M.; Hatch, N.A.; Marleau, F.R.; et al. Euclid: Early Release Observations—The surface brightness and colour profiles of the far outskirts of galaxies in the Perseus cluster. *Astron. Astrophys.* **2025**, *699*, A214. [CrossRef]
36. Chen, L.; Du, M.; Lu, S.; Li, J.; Ho, L.C. Down-bending Breaks in Galactic Disks Are an Intrinsic Byproduct of Inside-out Growth. *arXiv* **2026**, arXiv:2602.00626. [CrossRef]
37. Nelson, D.; Springel, V.; Pillepich, A.; Rodriguez-Gomez, V.; Torrey, P.; Genel, S.; Vogelsberger, M.; Pakmor, R.; Marinacci, F.; Weinberger, R.; et al. The IllustrisTNG simulations: Public data release. *Comput. Astrophys. Cosmol.* **2019**, *6*, 2. [CrossRef]
38. Erwin, P.; Beckman, J.E.; Pohlen, M. Antitruncation of Disks in Early-Type Barred Galaxies. *Astrophys. J.* **2005**, *626*, L81–L84. [CrossRef] [PubMed]
39. Bakos, J.; Trujillo, I. Deep Surface Brightness Profiles of Spiral Galaxies from SDSS Stripe82: Touching Stellar Halos. *arXiv* **2012**, arXiv:1204.3082. [CrossRef]
40. Maltby, D.T.; Gray, M.E.; Aragón-Salamanca, A.; Wolf, C.; Bell, E.F.; Jogee, S.; Häußler, B.; Barazza, F.D.; Böhm, A.; Jahnke, K. The environmental dependence of the structure of outer galactic discs in STAGES spiral galaxies. *Mon. Not. R. Astron. Soc.* **2012**, *419*, 669–686. [CrossRef]
41. Martín-Navarro, I.; Bakos, J.; Trujillo, I.; Knapen, J.H.; Athanassoula, E.; Bosma, A.; Comerón, S.; Elmegreen, B.G.; Erroz-Ferrer, S.; Gadotti, D.A.; et al. A unified picture of breaks and truncations in spiral galaxies from SDSS and S^4G imaging. *Mon. Not. R. Astron. Soc.* **2012**, *427*, 1102–1134. [CrossRef]
42. Dey, A.; Schlegel, D.J.; Lang, D.; Blum, R.; Burleigh, K.; Fan, X.; Findlay, J.R.; Finkbeiner, D.; Herrera, D.; Juneau, S.; et al. Overview of the DESI Legacy Imaging Surveys. *Astron. J.* **2019**, *157*, 168. [CrossRef]
43. Abdurro'uf; Accetta, K.; Aerts, C.; Silva Aguirre, V.; Ahumada, R.; Ajgaonkar, N.; Filiz Ak, N.; Alam, S.; Allende Prieto, C.; Almeida, A.; et al. The Seventeenth Data Release of the Sloan Digital Sky Surveys: Complete Release of MaNGA, MaStar, and APOGEE-2 Data. *Astrophys. J. Suppl. Ser.* **2022**, *259*, 35. [CrossRef]
44. van der Kruit, P.C.; Searle, L. Surface photometry of edge-on spiral galaxies. I—A model for the three-dimensional distribution of light in galactic disks. *Astron. Astrophys.* **1981**, *95*, 105–115.
45. Borlaff, A.; Eliche-Moral, M.C.; Beckman, J.; Font, J. Type-II surface brightness profiles in edge-on galaxies produced by flares. *Astron. Astrophys.* **2016**, *591*, L7. [CrossRef]
46. de Grijs, R. The global structure of galactic discs. *Mon. Not. R. Astron. Soc.* **1998**, *299*, 595–610. [CrossRef]
47. Kregel, M.; van der Kruit, P.C.; de Grijs, R. Flattening and truncation of stellar discs in edge-on spiral galaxies. *Mon. Not. R. Astron. Soc.* **2002**, *334*, 646–668. [CrossRef]

48. Pohlen, M.; Zaroubi, S.; Peletier, R.F.; Dettmar, R.J. On the three-dimensional structure of edge-on disc galaxies. *Mon. Not. R. Astron. Soc.* **2007**, *378*, 594–616. [CrossRef]
49. Bell, E.F.; McIntosh, D.H.; Katz, N.; Weinberg, M.D. The Optical and Near-Infrared Properties of Galaxies. I. Luminosity and Stellar Mass Functions. *Astrophys. J. Suppl. Ser.* **2003**, *149*, 289–312. [CrossRef]
50. Ebrová, I.; Bílek, M.; Eliášek, J. Photometric stellar masses for galaxies in DESI Legacy Imaging Surveys. *Astron. Astrophys.* **2025**, *704*, A232. [CrossRef]
51. Makarov, D.; Savchenko, S.; Mosenkov, A.; Bizyaev, D.; Reshetnikov, V.; Antipova, A.; Tikhonenko, I.; Usachev, P.; Borisov, S.; Makarova, L.; et al. The edge-on Galaxies in the Pan-STARRS survey (EGIPS). *Mon. Not. R. Astron. Soc.* **2022**, *511*, 3063–3075. [CrossRef]
52. Karachentsev, I.D.; Karachentseva, V.E.; Kudrya, Y.N.; Sharina, M.E.; Parnovskij, S.L. The revised Flat Galaxy Catalogue. *Bull. Spec. Astrophys. Obs.* **1999**, *47*, 5–185. [CrossRef]
53. Chambers, K.C.; Magnier, E.A.; Metcalfe, N.; Flewelling, H.A.; Huber, M.E.; Waters, C.Z.; Denneau, L.; Draper, P.W.; Farrow, D.; Finkbeiner, D.P.; et al. The Pan-STARRS1 Surveys. *arXiv* **2016**, arXiv:1612.05560. [CrossRef]
54. Bianchi, S. The dust distribution in edge-on galaxies. Radiative transfer fits of V and K′-band images. *Astron. Astrophys.* **2007**, *471*, 765–773. [CrossRef]
55. De Geyter, G.; Baes, M.; Camps, P.; Fritz, J.; De Looze, I.; Hughes, T.M.; Viaene, S.; Gentile, G. The distribution of interstellar dust in CALIFA edge-on galaxies via oligochromatic radiative transfer fitting. *Mon. Not. R. Astron. Soc.* **2014**, *441*, 869–885. [CrossRef]
56. Bertin, E.; Arnouts, S. SExtractor: Software for source extraction. *Astron. Astrophys. Suppl. Ser.* **1996**, *117*, 393–404. [CrossRef]
57. Joye, W.A.; Mandel, E. New Features of SAOImage DS9. In *Proceedings of the Astronomical Data Analysis Software and Systems XII*; Payne, H.E., Jedrzejewski, R.I., Hook, R.N., Eds.; Astronomical Society of the Pacific: San Francisco, CA, USA, 2003; Volume 295, p. 489.
58. Gadotti, D.A.; Baes, M.; Falony, S. Radiative transfer in disc galaxies—IV. The effects of dust attenuation on bulge and disc structural parameters. *Mon. Not. R. Astron. Soc.* **2010**, *403*, 2053–2062. [CrossRef]
59. Pastrav, B.A.; Popescu, C.C.; Tuffs, R.J.; Sansom, A.E. The effects of dust on the derived photometric parameters of disks and bulges in spiral galaxies. *Astron. Astrophys.* **2013**, *553*, A80. [CrossRef]
60. Pastrav, B.A.; Popescu, C.C.; Tuffs, R.J.; Sansom, A.E. The effects of dust on the photometric parameters of decomposed disks and bulges. *Astron. Astrophys.* **2013**, *557*, A137. [CrossRef]
61. Savchenko, S.S.; Poliakov, D.M.; Mosenkov, A.V.; Smirnov, A.A.; Marchuk, A.A.; Il'in, V.B.; Gontcharov, G.A.; Seguine, J.; Baes, M. The problem of dust attenuation in photometric decomposition of edge-on galaxies and possible solutions. *Mon. Not. R. Astron. Soc.* **2023**, *524*, 4729–4745. [CrossRef]
62. Bizyaev, D.; Kajsin, S. The Stellar Disk Thickness of Low Surface Brightness Galaxies. *Astrophys. J.* **2004**, *613*, 886–897. [CrossRef]
63. Gadotti, D.A. Robust galaxy image decompositions with differential evolution optimization and the problem of classical bulges in and beyond the nearby Universe. *Mon. Not. R. Astron. Soc.* **2026**, *545*, staf2072. [CrossRef]
64. Savchenko, S.S.; Sotnikova, N.Y.; Mosenkov, A.V.; Reshetnikov, V.P.; Bizyaev, D.V. Measuring the X-shaped structures in edge-on galaxies. *Mon. Not. R. Astron. Soc.* **2017**, *471*, 3261–3272. [CrossRef]
65. Smirnov, A.A.; Savchenko, S.S. New X-shaped bulge photometric model as a tool for measuring B/PS bulges and their X-structures in photometric studies. *Mon. Not. R. Astron. Soc.* **2020**, *499*, 462–481. [CrossRef]
66. Schlafly, E.F.; Finkbeiner, D.P. Measuring Reddening with Sloan Digital Sky Survey Stellar Spectra and Recalibrating SFD. *Astrophys. J.* **2011**, *737*, 103. [CrossRef]
67. López-Corredoira, M.; Cabrera-Lavers, A.; Garzón, F.; Hammersley, P.L. Old stellar Galactic disc in near-plane regions according to 2MASS: Scales, cut-off, flare and warp. *Astron. Astrophys.* **2002**, *394*, 883–899. [CrossRef]
68. de Grijs, R.; Peletier, R.F. The shape of galaxy disks: How the scale height increases with galactocentric distance. *Astron. Astrophys.* **1997**, *320*, L21–L24. [CrossRef]
69. Narayan, C.A.; Jog, C.J. Origin of radially increasing stellar scaleheight in a galactic disk. *Astron. Astrophys.* **2002**, *390*, L35–L38. [CrossRef]
70. Saha, K.; de Jong, R.; Holwerda, B. The onset of warps in Spitzer observations of edge-on spiral galaxies. *Mon. Not. R. Astron. Soc.* **2009**, *396*, 409–422. [CrossRef]
71. Kasparova, A.V.; Katkov, I.Y.; Chilingarian, I.V. An excessively massive thick disc of the enormous edge-on lenticular galaxy NGC 7572. *Mon. Not. R. Astron. Soc.* **2020**, *493*, 5464–5478. [CrossRef]
72. Hammersley, P.L.; López-Corredoira, M. Modelling star counts in the Monoceros stream and the Galactic anti-centre. *Astron. Astrophys.* **2011**, *527*, A6. [CrossRef]
73. López-Corredoira, M.; Molgó, J. Flare in the Galactic stellar outer disc detected in SDSS-SEGUE data. *Astron. Astrophys.* **2014**, *567*, A106. [CrossRef]
74. Bovy, J.; Rix, H.W.; Schlafly, E.F.; Nidever, D.L.; Holtzman, J.A.; Shetrone, M.; Beers, T.C. The Stellar Population Structure of the Galactic Disk. *Astrophys. J.* **2016**, *823*, 30. [CrossRef]

75. Mackereth, J.T.; Bovy, J.; Schiavon, R.P.; Zasowski, G.; Cunha, K.; Frinchaboy, P.M.; García Perez, A.E.; Hayden, M.R.; Holtzman, J.; Majewski, S.R.; et al. The age-metallicity structure of the Milky Way disc using APOGEE. *Mon. Not. R. Astron. Soc.* **2017**, *471*, 3057–3078. [CrossRef]
76. Comerón, S.; Salo, H.; Knapen, J.H. The Reports of Thick Discs' Deaths Are Greatly Exaggerated. Thick Discs Are NOT Artefacts Caused by Diffuse Scattered Light. *Astron. Astrophys.* **2018**, *610*, A5. [CrossRef]
77. Laine, J.; Laurikainen, E.; Salo, H.; Comerón, S.; Buta, R.J.; Zaritsky, D.; Athanassoula, E.; Bosma, A.; Muñoz-Mateos, J.C.; Gadotti, D.A.; et al. Morphology and environment of galaxies with disc breaks in the S^4G and NIRS0S. *Mon. Not. R. Astron. Soc.* **2014**, *441*, 1992–2012. [CrossRef]
78. Comerón, S.; Elmegreen, B.G.; Salo, H.; Laurikainen, E.; Athanassoula, E.; Bosma, A.; Knapen, J.H.; Gadotti, D.A.; Sheth, K.; Hinz, J.L.; et al. Breaks in Thin and Thick Disks of Edge-on Galaxies Imaged in the Spitzer Survey Stellar Structure in Galaxies (S^4G). *Astrophys. J.* **2012**, *759*, 98. [CrossRef]
79. Smirnov, A.; Marchuk, A.; Zozulia, V.; Sotnikova, N.; Savchenko, S. Boxy/Peanut Bulges: Comparative Analysis of EGIPS Galaxies and TNG50 Models. *Galaxies* **2026**, *14*, 4. [CrossRef]
80. Combes, F.; Sanders, R.H. Formation and properties of persisting stellar bars. *Astron. Astrophys.* **1981**, *96*, 164–173.
81. Raha, N.; Sellwood, J.A.; James, R.A.; Kahn, F.D. A dynamical instability of bars in disk galaxies. *Nature* **1991**, *352*, 411–412. [CrossRef]
82. Marchuk, A.A.; Smirnov, A.A.; Sotnikova, N.Y.; Bunakalya, D.A.; Savchenko, S.S.; Reshetnikov, V.P.; Usachev, P.A.; Tikhonenko, I.S.; Zozulia, V.D.; Zakharova, D.A. B/PS bulges in DESI Legacy edge-on galaxies—I. Sample building. *Mon. Not. R. Astron. Soc.* **2022**, *512*, 1371–1390. [CrossRef]
83. Jiang, L.; Fan, X.; Bian, F.; McGreer, I.D.; Strauss, M.A.; Annis, J.; Buck, Z.; Green, R.; Hodge, J.A.; Myers, A.D.; et al. The Sloan Digital Sky Survey Stripe 82 Imaging Data: Depth-optimized Co-adds over 300 deg^2 in Five Filters. *Astrophys. J. Suppl. Ser.* **2014**, *213*, 12. [CrossRef]
84. Sheth, K.; Regan, M.; Hinz, J.L.; Gil de Paz, A.; Menéndez-Delmestre, K.; Muñoz-Mateos, J.C.; Seibert, M.; Kim, T.; Laurikainen, E.; Salo, H.; et al. The Spitzer Survey of Stellar Structure in Galaxies (S4G). *Publ. Astron. Soc. Pac.* **2010**, *122*, 1397–1414. [CrossRef]
85. Makarov, D.; Prugniel, P.; Terekhova, N.; Courtois, H.; Vauglin, I. HyperLEDA. III. The catalogue of extragalactic distances. *Astron. Astrophys.* **2014**, *570*, A13. [CrossRef]
86. van der Kruit, P.C. The Stars and Gas in Outer Parts of Galaxy Disks: Extended or Truncated, Flat or Warped? In *Proceedings of the Formation and Evolution of Galaxy Disks*; Astronomical Society of the Pacific Conference Series; Funes, J.G., Corsini, E.M., Eds.; Astronomical Society of the Pacific: San Francisco, CA, USA, 2008; Volume 396, p. 173. [CrossRef]

Disclaimer/Publisher's Note: The statements, opinions and data contained in all publications are solely those of the individual author(s) and contributor(s) and not of MDPI and/or the editor(s). MDPI and/or the editor(s) disclaim responsibility for any injury to people or property resulting from any ideas, methods, instructions or products referred to in the content.